Available online at www.sciencedirect.com
ScienceDirect
Comput. Methods Appl. Mech. Engrg. 377 (2021) 113597
Computer methods in applied mechanics and engineering
www.elsevier.com/locate/cma

A novel decoupled second-order time marching scheme for the two-phase incompressible Navier–Stokes/Darcy coupled nonlocal Allen–Cahn model

Xiaofeng Yang

Department of Mathematics, University of South Carolina, Columbia, SC 29208, USA

Received 12 September 2020; received in revised form 15 November 2020; accepted 17 November 2020
Available online 18 February 2021

Abstract

We construct a novel second-order time marching scheme with the full decoupling structure to solve a highly coupled nonlinear two-phase fluid flow system consisting of the nonlocal mass-conserved Allen–Cahn equation where two types of flow regimes are considered (Navier–Stokes and Darcy). We achieve the full decoupled structure by introducing a nonlocal variable and designing an additional ordinary differential equation for it which plays the key role to maintain the unconditional energy stability. The whole scheme is built upon the pressure correction/ quadratization approach for the fluid equation and nonlinear double-well potential, respectively. At each time step, one only needs to solve several independent elliptic equations with constant coefficients illustrating the high practical efficiency. We strictly prove that the scheme satisfies the unconditional energy stability, and carry out various numerical simulations to prove its stability and accuracy numerically, such as spinodal decomposition and fingering instability due to the continuous injection flow, etc.

Keywords: Fully-decoupled; Phase-field; Conserved-Allen–Cahn; Navier–Stokes; Darcy; Unconditional energy stability

1. Introduction

This paper develops a new completely decoupled second-order time-marching numerical method for solving two-phase incompressible fluid flow systems, in which the moving interface is governed by the nonlocal mass-conserved Allen–Cahn-type phase-field model. To show the versatility of the decoupling method, we consider two types of fluid flow models, one of which is the Navier–Stokes equation, and the other is the Darcy equation confined in the Hele–Shaw cell. The phase-field method generally includes two gradient flow models, in which the first is the Cahn–Hilliard dynamics, and the second is the Allen–Cahn dynamics. The former can conserve the mass automatically while the latter cannot. The nonlocal conserved Allen–Cahn model (abbreviated as CAC) derived from [1] which had been widely used to simulate the two-phase fluid flow problems or other situations (cf. [2–11]), is a modified version of Allen–Cahn dynamics, where the shortcoming of non-conservation of mass is removed. Formally, the accurate mass conservation is realized through the use of a very simple technique in which a nonlocal term is added to eliminate mass variance caused by the chemical potential. Compared with other versions of the

E-mail address: xfyang@math.sc.edu.

https://doi.org/10.1016/j.cma.2020.113597
0045-7825/

mass-conserved Allen–Cahn type models (cf. [6,12–14]) or the fourth-order Cahn–Hilliard equation with automatic mass-conservation property, the CAC model proposed in [1] has some obvious advantages. First, it can achieve an accurate conserved mass like the Cahn–Hilliard equation, but it is relatively simple to solve because it is a second-order equation. Second, since it follows the law of energy dissipation, it is more suitable for the design of energy stable schemes

Remarkably, we recall there exist many effective methods for the two components of the flow-coupled phase-field models. For example, the well-known projection type methods can efficiently solve the incompressible Navier–Stokes equations and Darcy equations, see [15–24]. Numerous methods, e.g., stabilization method [25–30], convex splitting method [31–35], Invariant Energy Quadratization (IEQ) [36–39], Scalar Auxiliary Variable (SAV) method [40–42]), or others [43–49] compose a large pool to deal with the phase-field type models. However, after coupling the phase-field model with the flow field, the synthetic model (cf. [50–54]) turns to a highly coupled nonlinear dynamical system which is very challenging for algorithm developments especially the energy-stable schemes. In the model, the stiffness is not only from the small interfacial width in the phase-field equation, but also due to the nonlinear couplings between the phase-field variable and the velocity field through the advection and surface tension terms (abbreviated as *adv-surf*). For highly coupled nonlinear systems with large stiffness issue problems, the simple discretization for nonlinear terms may lead to fully coupled/nonlinear schemes with considerable instability, or suffer from expensive computational costs, which is the motivation to develop a stable scheme (especially a linear, fully-decoupled scheme that can maintain energy stability unconditionally is preferred). To this end, one of the most challenging problems in algorithm designs is how to find an appropriate discretization method for the *adv-surf* terms.

Here, we briefly review the numerical schemes of the coupled phase-field models with Navier–Stokes equations and Darcy equations. For the Navier–Stokes coupled phase-field model, as far as the author knows, the only available energy-stable fully-decoupled scheme was developed in [22,29,55], in which the way to achieve the full decoupling structure is to add a stabilization term to the explicit advection velocity term (abbreviated as *Stab*-method, see the details of the scheme (3.48) given in Remark 3.6). However, this decoupling type scheme is only first-order accurate in time, and it requires more calculations at each time step because the scheme for the phase-field model has variable coefficients. For the Darcy coupled phase-field model, the situation is much better (in terms of accuracy) and a second-order fully-decoupled scheme was developed in [23], in which the *adv-surf* terms are discretized through explicit and implicit combination method (abbreviated as *Exp–Imp* method, see the details of the scheme (3.66)–(3.67) given in Remark 3.7). It should be emphasized that for the Navier–Stokes coupling system, the *Exp–Imp* method can only generate a fully-coupled scheme, see [24,35,56–62]. Hence, a natural question arises: why can we get a fully-decoupled scheme when using the *Exp–Imp* method to deal with the Darcy coupling model, but can only get a fully-coupled scheme when using the same method to deal with the Navier–Stokes coupling model?

The answer is due to the special format of the Darcy equation, where the pressure gradient and the velocity field satisfy an explicit linear relationship that does not involve any spatial derivatives. Therefore, one can use the pressure gradient and surface tension to express the fluid velocity explicitly and linearly, thereby achieving a completely decoupled type of scheme. However, if we use the same method to process the Navier–Stokes equation, the advective and viscous terms containing spatial derivatives will prevent us from obtaining similar linear relationships, so we cannot obtain a fully-decoupled scheme. Moreover, although the scheme given in [23] is fully-decoupled, there is some other notable shortcoming. For example, its computational cost is high because it needs to solve the phase-field equation with variable coefficients at each time step (see Fig. 4.3).

Therefore, the focus of this paper to develop a scheme that maintains energy stability unconditionally and the second-order time accuracy, while also achieving the full decoupling calculations. We expect this scheme is not only suitable for the Darcy coupling model, but also for the Navier–Stokes coupling model. Meanwhile, when the novel scheme is applied to either Navier–Stokes or Darcy coupled model, we hope that compared with the scheme in [23] that requires solving the variable-coefficient equations, the schemes given in this article are more efficient, that is, only the constant-coefficient equations are needed to be solved. To this goal, when developing numerical algorithms, we do not intend to use the specific form of the Darcy equation, but instead, turn our attention to using the obvious but usually ignored property of "*zero-energy-contribution*" satisfied by the *adv-surf* terms. In other words, it can be seen easily that the *adv-surf* terms do not impact the total free energy or energy diffusivity, which means their contribution to the free energy is zero. This is a well-known property, but it has never been used to design numerical algorithms. In this paper, we introduce a nonlocal variable and apply this property to

design a special ordinary differential equation (ODE) that contains the inner products of the *adv-surf* terms with some specific functions. In this way, the system can be rewritten into a new form, and the *adv-surf* terms can be discretized in a simple explicit manner. The original system and the newly modified system are equivalent, because the added ODE is trivial at the continuous level and all items contained in it are zero. But after discretization, the new variable and its associated ODE will play a key role. First, the ODE can help eliminate all the troublesome nonlinear terms to obtain provable stability. Second, the nonlocal property of the new variable can be used to decompose each unknown variable into a linear combination form and thus all equations can be decomposed into multiple independent equations, thereby obtaining a fully-decoupled structure.

This decoupling method is then combined other proven effective methods (projection/SAV methods) to form the expected scheme. The implementation of this scheme is very simple. It only needs to solve a few linear independent elliptic equations with constant coefficients at each time step, which means that computation is very efficient. We also give a rigorous proof of the solvability and unconditional energy stability of the scheme and further simulate various numerical examples in 2D and 3D to show its numerical effectiveness. In addition to the above-mentioned benefits, another important advantage of the new decoupling method is that it is universally applicable. For instance, first, it can be combined with other linear methods (such as the linear stabilization, IEQ methods, etc.) to form various types of fully-decoupled energy-stable schemes. Second, it can also be applied to any nonlinear coupling type model to form an effective full decoupling scheme (especially gradient flow type models coupled with other fields), for example, the temperature-coupled dendritic crystal growth model [63,64], the magnetic/electric-coupled model [65–67], the flow-coupled nematic/smectic liquid crystal model [68–70], etc.

We organize the rest of this article as follows. We briefly introduce the two models in Section 2, namely the Navier–Stokes equations coupled with the CAC model (NS-CAC, for short) and the Darcy equations coupled with the CAC model (D-CAC, for short). In Section 3, numerical schemes are constructed for solving these two models and introduce the practical implementation process in detail. We prove the unconditional energy stability rigorously (implementation and solvability are given in the Appendix). In Section 4, we implement the numerical simulations numerically to demonstrate the stability, accuracy of the developed schemes. In Section 5, we give some concluding remarks.

2. NS-CAC model and D-CAC model

We first briefly introduce the two models, the NS-CAC model, and the D-CAC model. Both models have been often applied to simulate the two-phase flow system, where the latter focuses on the fluid dynamics in porous media.

We introduce some notations here. The L^2 inner product of any two functions $\phi(\boldsymbol{x})$ and $\psi(\boldsymbol{x})$ is expressed as $(\phi(\boldsymbol{x}), \psi(\boldsymbol{x})) = \int_\Omega \phi(\boldsymbol{x})\psi(\boldsymbol{x})d\boldsymbol{x}$, and the L^2 norm of $\phi(\boldsymbol{x})$ is denoted as $\|\phi\|^2 = (\phi, \phi)$.

2.1. NS-CAC model

Suppose that Ω is a smooth, bounded, and connected domain in $\mathbb{R}^d$, $d = 2, 3$. We define $\phi(\boldsymbol{x}, t)$ as a phase-field variable (macro labeling function) to represent the mass (or volume) fraction of two different fluid components in the fluid mixture, i.e.,

$$\phi(x,t) = \begin{cases} 1 & \text{fluid 1,} \\ -1 & \text{fluid 2.} \end{cases} \tag{2.1}$$

The discontinuity between the two distinct values ± 1 is smoothed by a thin transition region of width $O(\epsilon)$ where $\epsilon \ll 1$. In terms of the variable ϕ and the average velocity field $\mathbf{u}$ for the fluid mixture, the postulated total free energy reads as

$$E(\mathbf{u}, \phi) = \int_\Omega \Big(\frac{1}{2}|\mathbf{u}|^2 + \lambda(\frac{1}{2}|\nabla\phi|^2 + F(\phi))\Big)d\boldsymbol{x}, \tag{2.2}$$

which is a combination of the kinetic energy, gradient potential, and the Ginzburg–Landau functional. Here, the nonlinear potential $F(\phi)$ is chosen to be the double-well form, i.e., $F(\phi) = \frac{1}{4\epsilon^2}(\phi^2 - 1)^2$, λ is related to the surface tension parameter, and the surface tension is defined as $\frac{2\sqrt{2}}{3}\frac{\lambda}{\epsilon}$, see [71].

Then, by applying the L^2 gradient flow method to the total free energy (that is, the Allen–Cahn relaxation dynamics), the NS-CAC model reads as:

$$\phi_t + \nabla\cdot(\mathbf{u}\phi) + M\Big(\mu - \frac{1}{|\Omega|}\int_\Omega \mu d\boldsymbol{x}\Big) = 0, \tag{2.3}$$

$$\mu = \lambda(-\Delta\phi + f(\phi)), \tag{2.4}$$

$$\mathbf{u}_t + (\mathbf{u}\cdot\nabla)\mathbf{u} - \nu\Delta\mathbf{u} + \nabla p + \phi\nabla\mu = 0, \tag{2.5}$$

$$\nabla\cdot\mathbf{u} = 0, \tag{2.6}$$

where M, ν, λ are all positive parameters, M is the mobility parameter, p is the pressure, ν is the fluid viscosity, $f(\phi) = F'(\phi) = \frac{1}{\epsilon^2}(\phi^3 - \phi)$, $\mu = \frac{\delta E}{\delta\phi}$ is the variational derivative or chemical potential, and the nonlocal term $-\frac{1}{|\Omega|}\int_\Omega \mu d\boldsymbol{x}$ is added in (2.3) to eliminate the total variance of mass (cf. [1]). We assume the boundary conditions are either periodic or

$$\mathbf{u}|_{\partial\Omega} = \mathbf{0}, \partial_{\mathbf{n}}\phi|_{\partial\Omega} = 0, \tag{2.7}$$

where $\mathbf{n}$ is the unit outward normal on the boundary $\partial\Omega$. The initial conditions read as

$$\mathbf{u}|_{(t=0)} = \mathbf{u}^0,\ p|_{(t=0)} = p^0\,, \phi|_{(t=0)} = \phi^0. \tag{2.8}$$

One can easily obtain mass conservation property for the model. By taking the L^2 inner product of (2.3) with 1, and applying the divergence theorem and the boundary conditions (2.7), the mass conservation property reads as:

$$\frac{d}{dt}\int_\Omega \phi d\boldsymbol{x} = 0. \tag{2.9}$$

It is also easy to see that the system (2.3)–(2.6) follows a dissipation law of energy by performing the following process of energy estimate. We multiply the inner product of (2.3) by μ in L^2 to derive

$$(\phi_t, \mu) = -M\Big\|\mu - \frac{1}{|\Omega|}\int_\Omega \mu d\boldsymbol{x}\Big\|^2 - \int_\Omega \nabla\cdot(\mathbf{u}\phi)\mu d\boldsymbol{x}, \tag{2.10}$$

where we use

$$\begin{aligned}
&(\mu - \frac{1}{|\Omega|}\int_\Omega \mu d\boldsymbol{x}, \mu)\\
&= (\mu - \frac{1}{|\Omega|}\int_\Omega \mu d\boldsymbol{x}, \mu - \frac{1}{|\Omega|}\int_\Omega \mu d\boldsymbol{x}) + (\mu - \frac{1}{|\Omega|}\int_\Omega \mu d\boldsymbol{x}, \frac{1}{|\Omega|}\int_\Omega \mu d\boldsymbol{x})\\
&= \Big\|\mu - \frac{1}{|\Omega|}\int_\Omega \mu d\boldsymbol{x}\Big\|^2,
\end{aligned}$$

since $(\mu - \frac{1}{|\Omega|}\int_\Omega \mu d\boldsymbol{x}, \frac{1}{|\Omega|}\int_\Omega \mu d\boldsymbol{x}) = 0$. Taking the inner product of (2.4) with $-\phi_t$ in L^2 and using integration by parts, we get

$$-(\mu, \phi_t) = -\frac{d}{dt}\int_\Omega (\frac{\lambda}{2}|\nabla\phi|^2 + \lambda F(\phi))d\boldsymbol{x}. \tag{2.11}$$

Taking the inner product of (2.5) with $\mathbf{u}$ in L^2, using integration by parts and (2.6), we obtain

$$\frac{d}{dt}\int_\Omega \frac{1}{2}|\mathbf{u}|^2 d\boldsymbol{x} + \|\sqrt{\nu}\nabla\mathbf{u}\|^2 + \int_\Omega \Big(\phi\nabla\mu\cdot\mathbf{u} + (\mathbf{u}\cdot\nabla)\mathbf{u}\cdot\mathbf{u}\Big)d\boldsymbol{x} = 0. \tag{2.12}$$

Combining the above three Eqs. (2.10)–(2.12) and noticing some terms are canceled out, we obtain the energy law as follows:

$$\frac{d}{dt}E(\mathbf{u}, \phi) = -M\Big\|\mu - \frac{1}{|\Omega|}\int_\Omega \mu d\boldsymbol{x}\Big\|^2 - \|\sqrt{\nu}\nabla\mathbf{u}\|^2, \tag{2.13}$$

where two of the negative terms specify the diffusion rate of the total free energy $E(\mathbf{u}, \phi)$.

Remarkably, during the process of obtaining the energy law (2.13), the two integrals originated from the advection and surface tension terms finally vanish due to the following two identities hold:

$$\int_\Omega \big(\phi\nabla\mu\cdot\mathbf{u} + \nabla\cdot(\mathbf{u}\phi)\mu\big)d\boldsymbol{x} = 0, \quad \int_\Omega (\mathbf{u}\cdot\nabla)\mathbf{u}\cdot\mathbf{u}d\boldsymbol{x} = 0. \tag{2.14}$$

One can easily verify the above two equalities by using integration by parts, (2.6) and (2.7). The final disappearance of these nonlinear terms can be regarded as they do not impact the total free energy of the system. Therefore, we refer them as "*zero-energy-contribution*" terms. In next subsection, this well-known but often overlooked property will be used to develop the numerical scheme with full decoupling structure.

2.2. D-CAC model

The D-CAC model follows the same framework as the NS-CAC model expect that the fluid momentum equation follows the Darcy's law. The D-CAC model reads as

$$\phi_t + \nabla \cdot (\mathbf{u}\phi) + M\Big(\mu - \frac{1}{|\Omega|}\int_\Omega \mu d\boldsymbol{x}\Big) = 0, \tag{2.15}$$

$$\mu = \lambda(-\Delta\phi + f(\phi)), \tag{2.16}$$

$$\tau \mathbf{u}_t + \alpha\nu\mathbf{u} + \nabla p + \phi\nabla\mu = 0, \tag{2.17}$$

$$\nabla \cdot \mathbf{u} = 0, \tag{2.18}$$

where $\mathbf{u}$ represents the nondimensionalized seepage velocity, τ is a positive parameter, $\alpha > 0$ is the dimensionless hydraulic conductivity. Note the time derivative of the seepage velocity $\mathbf{u}$ is retained for flows in porous medium, cf. [23,24,72,73].

The boundary conditions are either periodic or

$$\mathbf{u}\cdot\mathbf{n}|_{\partial\Omega} = \partial_{\mathbf{n}}\phi|_{\partial\Omega} = 0. \tag{2.19}$$

The initial conditions read as

$$\phi|_{(t=0)} = \phi^0,\ \mathbf{u}|_{(t=0)} = \mathbf{u}^0,\ p|_{(t=0)} = p^0. \tag{2.20}$$

The D-CAC system (2.15)–(2.18) also follows energy dissipation property. Since the derivation process is quite similar to the NS-CAC model, we omit the details and only present the energy law is as follows:

$$\frac{d}{dt}\mathscr{E}(\mathbf{u},\phi) = -M\Big\|\mu - \frac{1}{|\Omega|}\int_\Omega \mu d\boldsymbol{x}\Big\|^2 - \alpha\|\sqrt{\nu}\mathbf{u}\|^2, \tag{2.21}$$

where the two negative terms on the right end specify the diffusion rate of the total free energy, and the total energy reads as

$$\mathscr{E}(\mathbf{u},\phi) = \int_\Omega \Big(\frac{\tau}{2}|\mathbf{u}|^2 + \lambda(\frac{1}{2}|\nabla\phi|^2 + F(\phi))\Big)d\boldsymbol{x}. \tag{2.22}$$

3. Numerical scheme

In this section, we develop numerical schemes for the two coupled nonlinear systems, the NS-CAC model (2.3)–(2.6) and the D-CAC model (2.15)–(2.18).

3.1. NS-CAC model

3.1.1. Reformulation

We introduce a nonlocal variable $Q(t)$ and an ODE system related to it, that reads as:

$$\begin{cases} Q_t = \displaystyle\int_\Omega (\nabla\cdot(\mathbf{u}\phi)\mu + (\phi\nabla\mu)\cdot\mathbf{u} + (\mathbf{u}\cdot\nabla)\mathbf{u}\cdot\mathbf{u})\,d\boldsymbol{x}, \\ \nabla\cdot\mathbf{u} = 0, \\ Q|_{(t=0)} = 1, \\ \mathbf{u}|_{\partial\Omega} = \mathbf{0} \text{ or all variables are periodic.} \end{cases} \tag{3.1}$$

By utilizing the "*zero-energy-contribution*" property (2.14) satisfied by the *adv-surf* terms, it is easy to derive that the ODE (3.1) is equivalent to an ODE ($Q_t = 0$, $Q|_{(t=0)} = 1$) with the trivial solution of $Q(t) = 1$.

We introduce another nonlocal auxiliary variable $U(t)$ such that

$$U(t) = \sqrt{\int_\Omega (F(\phi) - \frac{s}{2\epsilon^2}\phi^2)d\boldsymbol{x} + B}, \tag{3.2}$$

where s is a positive stabilization parameter, and B is a constant to guarantee that the radicand is positive. Note that $F(\phi)$ is a quartic polynomial, so no matter how big s is, the term $\int_\Omega (F(\phi) - \frac{s}{2\epsilon^2}\phi^2)d\boldsymbol{x}$ can always be guaranteed to be bounded from below.

Then, by using the two variables Q and U, and combining the ODE (3.1) with the NS-CAC system (2.3)–(2.6), we get a modified system as:

$$\phi_t + Q\nabla\cdot(\mathbf{u}\phi) = -M\left(\mu - \frac{1}{|\Omega|}\int_\Omega \mu d\boldsymbol{x}\right), \tag{3.3}$$

$$\mu = \lambda(-\Delta\phi + \frac{s}{\epsilon^2}\phi + HU), \tag{3.4}$$

$$U_t = \frac{1}{2}\int_\Omega H\phi_t d\boldsymbol{x}, \tag{3.5}$$

$$\mathbf{u}_t + Q(\mathbf{u}\cdot\nabla)\mathbf{u} - \nu\Delta\mathbf{u} + \nabla p + Q\phi\nabla\mu = 0, \tag{3.6}$$

$$\nabla\cdot\mathbf{u} = 0, \tag{3.7}$$

$$Q_t = \int_\Omega \Big(\nabla\cdot(\mathbf{u}\phi)\mu + (\phi\nabla\mu)\cdot\mathbf{u} + (\mathbf{u}\cdot\nabla)\mathbf{u}\cdot\mathbf{u}\Big)d\boldsymbol{x}, \tag{3.8}$$

where

$$H(\phi) = \frac{f(\phi) - \frac{s}{\epsilon^2}\phi}{\sqrt{\int_\Omega (F(\phi) - \frac{s}{2\epsilon^2}\phi^2)d\boldsymbol{x} + B}}. \tag{3.9}$$

The transformed system (3.3)–(3.8) satisfies the following initial conditions,

$$\begin{aligned} &\mathbf{u}|_{(t=0)} = \mathbf{u}^0,\ p|_{(t=0)} = p^0,\ \phi|_{(t=0)} = \phi^0, \\ &Q|_{(t=0)} = 1,\ U|_{(t=0)} = \sqrt{\int_\Omega (F(\phi^0) - \frac{s}{2\epsilon^2}(\phi^0)^2)d\boldsymbol{x} + B}. \end{aligned} \tag{3.10}$$

and the boundary conditions are either periodic or

$$\mathbf{u}|_{\partial\Omega} = \mathbf{0},\ \partial_{\mathbf{n}}\phi|_{\partial\Omega} = 0, \tag{3.11}$$

In the next two comments, we will give some detailed explanations of the above reformulation.

Remark 3.1. When we combine the ODE (3.8) with the original system (2.3)–(2.6), we make some modifications to the resulting model. The first modification is made to the chemical potential μ, in which the nonlocal variable U is used, and (3.6) is obtained by taking the time derivative for U. This modification will not change the system, because we can restore the chemical potential (2.4) by integrating (3.6) over time. The second modification is made to the *adv-surf* terms where we multiply them by Q. Since the variable Q is equal to 1, the PDE system is not changed by this modification as well. In summary, the above description illustrates the equivalence between the two PDE systems, (2.3)–(2.6) and (3.3)–(3.8).

Remark 3.2. The modified system (3.3)–(3.8) still holds the property of mass conservation. By taking the L^2 inner product of (3.3) with 1, and using the nonlocal property of the variable Q, we get

$$\int_\Omega Q\nabla\cdot(\mathbf{u}\phi)d\boldsymbol{x} = Q\int_\Omega \nabla\cdot(\mathbf{u}\phi)d\boldsymbol{x} = 0, \tag{3.12}$$

which is due the boundary condition $\mathbf{u}\cdot\mathbf{n}|_{\partial\Omega} = 0$. This means $\frac{d}{dt}\int_\Omega \phi d\boldsymbol{x} = 0$, that is, the mass is conserved over time. Moreover, for the discrete scheme, since the discrete solution of Q is also nonlocal, as long as the numerical solution of $\mathbf{u}$ has a similar boundary condition, the mass conservation property of the discrete solution of ϕ still holds.

The transformed system (3.3)–(3.8) also follows an energy dissipative law that can be derived by a similar procedure to obtain (2.13). We present the detailed process since the energy stability proof in the discrete level follows the same line.

By taking the L^2 inner product of (3.3) with μ, we derive

$$(\phi_t, \mu) + Q\int_\Omega \nabla\cdot(\mathbf{u}\phi)\mu d\boldsymbol{x} = -M\left\|\mu - \frac{1}{|\Omega|}\int_\Omega \mu d\boldsymbol{x}\right\|^2. \tag{3.13}$$

By taking the L^2 inner product of (3.4) with ϕ_t, we obtain

$$-(\mu, \phi_t) + \lambda\frac{d}{dt}\int_\Omega\left(\frac{1}{2}|\nabla\phi|^2 + \frac{s}{2\epsilon^2}|\phi|^2\right)d\boldsymbol{x} + \lambda U\int_\Omega H\phi_t d\boldsymbol{x} = 0. \tag{3.14}$$

By taking the L^2 inner product of (3.5) with $2\lambda U$, we obtain

$$\lambda\frac{d}{dt}(|U|^2) - \lambda U\int_\Omega H\phi_t d\boldsymbol{x} = 0. \tag{3.15}$$

By taking the L^2 inner product of (3.6) with $\mathbf{u}$ and using (3.7), we obtain

$$\frac{d}{dt}\int_\Omega\frac{1}{2}|\mathbf{u}|^2 d\boldsymbol{x} + \nu\|\nabla\mathbf{u}\|^2 + Q\int_\Omega \mathbf{u}\cdot\nabla\mathbf{u}\cdot\mathbf{u}d\boldsymbol{x} + Q\int_\Omega\phi\nabla\mu\cdot\mathbf{u}d\boldsymbol{x} = 0. \tag{3.16}$$

By multiplying (3.8) with Q, we obtain

$$\frac{d}{dt}\left(\frac{|Q|^2}{2}\right) = Q\int_\Omega\Big(\nabla\cdot(\mathbf{u}\phi)\mu + (\phi\nabla\mu)\cdot\mathbf{u} + (\mathbf{u}\cdot\nabla)\mathbf{u}\cdot\mathbf{u}\Big)d\boldsymbol{x}. \tag{3.17}$$

By combining the above five equalities and noticing that the three nonlocal terms with Q in (3.13) and (3.16) are canceled by the three nonlocal terms in (3.17), we obtain the energy law as follows,

$$\begin{aligned}\frac{d}{dt}\left(\int_\Omega\Big(\frac{1}{2}|\mathbf{u}|^2 + \frac{\lambda}{2}|\nabla\phi|^2 + \frac{\lambda s}{2\epsilon^2}|\phi|^2\Big)d\boldsymbol{x} + \lambda|U|^2 + \frac{|Q|^2}{2}\right)\\ = -M\left\|\mu - \frac{1}{|\Omega|}\int_\Omega\mu d\boldsymbol{x}\right\|^2 - \|\sqrt{\nu}\nabla\mathbf{u}\|^2 \le 0.\end{aligned} \tag{3.18}$$

3.1.2. Decoupled numerical scheme for the NS-CAC model

Now we develop a numerical scheme for (3.3)–(3.8) based on the second-order backward differential formula (BDF2) as follows. Let ψ^n be the numerical approximation to the analytic function $\psi(\cdot,t)|_{t=t^n}$. Let $\delta t > 0$ be a time step size and set $t^n = n\delta t$ for $0 \le n \le N$ with $T = N\delta t$.

Assuming $(\tilde{\mathbf{u}}, \mathbf{u}, p, \phi, \mu, Q, U)^n$ and $(\tilde{\mathbf{u}}, \mathbf{u}, p, \phi, \mu, Q, U)^{n-1}$ are known, we update $(\tilde{\mathbf{u}}, \mathbf{u}, p, \phi, \mu, Q, U)^{n+1}$ by

$$\frac{a\phi^{n+1} - b\phi^n + c\phi^{n-1}}{2\delta t} + Q^{n+1}\nabla\cdot(\mathbf{u}^*\phi^*) = -M\left(\mu^{n+1} - \frac{1}{|\Omega|}\int_\Omega\mu^{n+1}d\boldsymbol{x}\right), \tag{3.19}$$

$$\mu^{n+1} = \lambda(-\Delta\phi^{n+1} + \frac{s}{\epsilon^2}\phi^{n+1} + H^*U^{n+1}), \tag{3.20}$$

$$aU^{n+1} - bU^n + cU^{n-1} = \frac{1}{2}\int_\Omega H^*(3\phi^{n+1} - 4\phi^n + \phi^{n-1})d\boldsymbol{x}, \tag{3.21}$$

$$\frac{a\tilde{\mathbf{u}}^{n+1} - b\mathbf{u}^n + c\mathbf{u}^{n-1}}{2\delta t} + Q^{n+1}(\mathbf{u}^*\cdot\nabla)\mathbf{u}^* - \nu\Delta\tilde{\mathbf{u}}^{n+1} + \nabla p^n + Q^{n+1}\phi^*\nabla\mu^* = 0, \tag{3.22}$$

$$\frac{aQ^{n+1} - bQ^n + cQ^{n-1}}{2\delta t} = \int_\Omega\Big(\nabla\cdot(\mathbf{u}^*\phi^*)\mu^{n+1} + (\phi^*\nabla\mu^*)\cdot\tilde{\mathbf{u}}^{n+1} + (\mathbf{u}^*\cdot\nabla)\mathbf{u}^*\cdot\tilde{\mathbf{u}}^{n+1}\Big)d\boldsymbol{x}, \tag{3.23}$$

and

$$\frac{a}{2\delta t}(\mathbf{u}^{n+1} - \tilde{\mathbf{u}}^{n+1}) + \nabla(p^{n+1} - p^n) = 0, \tag{3.24}$$

$$\nabla\cdot\mathbf{u}^{n+1} = 0, \tag{3.25}$$

where

$$\begin{aligned}&a = 3, b = 4, c = 1, \mathbf{u}^* = 2\mathbf{u}^n - \mathbf{u}^{n-1}, \phi^* = 2\phi^n - \phi^{n-1},\\ &\mu^* = 2\mu^n - \mu^{n-1}, H^* = H(\phi^*).\end{aligned} \tag{3.26}$$

The boundary conditions for the unknown variables $\mathbf{u}^{n+1}$, $\tilde{\mathbf{u}}^{n+1}$ and ϕ^{n+1} are either periodic or the following

$$\tilde{\mathbf{u}}^{n+1}|_{\partial\Omega} = \mathbf{0}, \mathbf{u}^{n+1}\cdot\mathbf{n}|_{\partial\Omega} = \partial_{\mathbf{n}}\phi^{n+1}|_{\partial\Omega} = 0. \tag{3.27}$$

We give the details on how to obtain the decoupling structure and implementation details, see Appendix A.1. In the following remarks, we give some detailed descriptions of the above scheme.

Remark 3.3. The computations of the second-order scheme (3.19)–(3.25) require all values of $t = t^1$. In practice, we can obtain these values by constructing a similar first-order scheme based on the backward Euler method (e.g. setting $a = 2, b = 2, c = 0, \psi^* = \psi^0, \forall\psi$, the scheme becomes first order). Meanwhile, similar to the continuous case, the mass-conserved property of ϕ^{n+1} still holds. By taking the L^2 inner product with 1 for (3.19), using integration by parts, the boundary condition of $\mathbf{u}^*\cdot\mathbf{n}|_{\partial\Omega} = 0$, and noticing that Q^{n+1} is a nonlocal scalar, we derive $\int_\Omega \phi^{n+1}d\boldsymbol{x} = \int_\Omega \frac{b\phi^n - c\phi^{n-1}}{a}d\boldsymbol{x}$. By using the math induction (since it is easy to derive $\int_\Omega \phi^1 d\boldsymbol{x} = \int_\Omega \phi^0 d\boldsymbol{x}$ from the first-order scheme), it is easy to obtain $\int_\Omega \phi^{n+1}d\boldsymbol{x} = \int_\Omega \phi^n d\boldsymbol{x} = \cdots = \int_\Omega \phi^0 d\boldsymbol{x}$.

Remark 3.4. We use the second-order pressure-correction method to solve the Navier–Stokes equations. In this way, the calculation of the pressure is separated from the calculation of the velocity field. The variable $\tilde{\mathbf{u}}$ is an intermediate velocity field that only meets the homogeneous Dirichlet boundary condition but does not verify the divergence-free condition. (3.24)–(3.25) is the projection step to obtain the final velocity field $\mathbf{u}^{n+1}$, which is divergence-free, but only partially meets the homogenous Dirichlet boundary condition. To solve the pressure p^{n+1} and $\mathbf{u}^{n+1}$, by applying the divergence operator $\nabla\cdot$ to (3.24) and using the divergence-free conditions for $\mathbf{u}^{n+1}$, then the following Poisson equation for p^{n+1} with the periodic boundary conditions or homogenous Neumann boundary conditions, is obtained, i.e.,

$$-\Delta p^{n+1} = -\frac{3}{2\delta t}\nabla\cdot\tilde{\mathbf{u}}^{n+1} - \Delta p^n. \tag{3.28}$$

Once p^{n+1} is computed from (3.28), we update $\mathbf{u}^{n+1}$ by using (3.24), i.e.,

$$\mathbf{u}^{n+1} = \tilde{\mathbf{u}}^{n+1} - \frac{2\delta t}{3}\nabla(p^{n+1} - p^n). \tag{3.29}$$

Remark 3.5. Energy stability can be improved by effectively using the stabilization term (the term related to s in (3.20)). This had been demonstrated by numerous numerical tests given in [74,75] for a series of phase-field models with high stiffness while using larger time steps for simulations. For models with very high stiffness issue due to the model parameters or strong anisotropy so that spatial oscillations can induce severe constraints on the time step, while the SAV method applied to these models are formally unconditionally energy stable, but exceedingly small time steps are needed to achieve reasonable accuracy. To fix such an inherent deficiency, the stabilization technique is often combined with the SAV method to form the so-called stabilized-SAV (S-SAV) method. More precisely, by adding one or several suitable linear stabilization terms and treating involved nonlinear terms in a semi-explicit way, we can construct an unconditionally energy stable scheme which is easy to solve and can produce accurate results with reasonable time steps. About the details of how to apply various effective stabilization terms to different highly stiff models, we refer to some recent review works in [74,75].

3.1.3. Unconditional energy stability

Now we prove that the scheme (3.19)–(3.25) is unconditionally energy stable as follows.

Theorem 3.1. *The time-discrete scheme (3.19)–(3.25) satisfies the discrete energy dissipation law as follows*

$$\frac{1}{\delta t}(E^{n+1} - E^{n-1}) \le -\|\sqrt{\nu}\nabla\tilde{\mathbf{u}}^{n+1}\|^2 - M\left\|\mu^{n+1} - \frac{1}{|\Omega|}\int_\Omega \mu^{n+1}d\boldsymbol{x}\right\|^2 \le 0, \tag{3.30}$$

where

$$\begin{aligned} E^{n+1} =& \frac{1}{2}\Big(\frac{1}{2}\|\mathbf{u}^{n+1}\|^2+\frac{1}{2}\|2\mathbf{u}^{n+1}-\mathbf{u}^{n}\|^2\Big)+\frac{\delta t^2}{3}\|\nabla p^{n+1}\|^2 \\ &+\frac{\lambda}{2}(\frac{1}{2}\|\nabla\phi^{n+1}\|^2+\frac{1}{2}\|2\nabla\phi^{n+1}-\nabla\phi^{n}\|^2) \\ &+\frac{\lambda s}{2\epsilon^2}(\frac{1}{2}\|\phi^{n+1}\|^2+\frac{1}{2}\|2\phi^{n+1}-\phi^{n}\|^2) \\ &+\lambda(\frac{1}{2}|U^{n+1}|^2+\frac{1}{2}|2U^{n+1}-U^{n}|^2)+\frac{1}{2}(\frac{1}{2}|Q^{n+1}|^2+\frac{1}{2}|2Q^{n+1}-Q^{n}|^2). \end{aligned} \tag{3.31}$$

Proof. After taking the inner product of (3.22) with $2\delta t\tilde{\mathbf{u}}^{n+1}$ in the L^2 space, we arrive at the following equation:

$$\begin{aligned} &(3\tilde{\mathbf{u}}^{n+1}-4\mathbf{u}^{n}+\mathbf{u}^{n-1},\tilde{\mathbf{u}}^{n+1})+2\delta t\|\sqrt{\nu}\nabla\tilde{\mathbf{u}}^{n+1}\|^2+2\delta t(\nabla p^{n},\tilde{\mathbf{u}}^{n+1}) \\ &\quad+2\delta t\,Q^{n+1}\left(\int_\Omega(\mathbf{u}^*\cdot\nabla)\mathbf{u}^*\cdot\tilde{\mathbf{u}}^{n+1}d\boldsymbol{x}+\int_\Omega(\phi^*\nabla\mu^*)\cdot\tilde{\mathbf{u}}^{n+1}d\boldsymbol{x}\right)=0. \end{aligned} \tag{3.32}$$

From (3.24), for any variable $\mathbf{v}$ with $\nabla\cdot\mathbf{v}=0$ and $\mathbf{v}\cdot\mathbf{n}|_{\partial\Omega}=0$, we have

$$(\mathbf{u}^{n+1},\mathbf{v})=(\tilde{\mathbf{u}}^{n+1},\mathbf{v}). \tag{3.33}$$

We derive following equality

$$\begin{aligned} &(3\tilde{\mathbf{u}}^{n+1}-4\mathbf{u}^{n}+\mathbf{u}^{n-1},\tilde{\mathbf{u}}^{n+1}) \\ &\quad=(3\tilde{\mathbf{u}}^{n+1}-4\mathbf{u}^{n}+\mathbf{u}^{n-1},\mathbf{u}^{n+1})+(3\tilde{\mathbf{u}}^{n+1}-4\mathbf{u}^{n}+\mathbf{u}^{n-1},\tilde{\mathbf{u}}^{n+1}-\mathbf{u}^{n+1}) \\ &\quad=(3\mathbf{u}^{n+1}-4\mathbf{u}^{n}+\mathbf{u}^{n-1},\mathbf{u}^{n+1})+(3\tilde{\mathbf{u}}^{n+1},\ \tilde{\mathbf{u}}^{n+1}-\mathbf{u}^{n+1}) \\ &\quad=(3\mathbf{u}^{n+1}-4\mathbf{u}^{n}+\mathbf{u}^{n-1},\mathbf{u}^{n+1})+3(\tilde{\mathbf{u}}^{n+1}+\mathbf{u}^{n+1},\tilde{\mathbf{u}}^{n+1}-\mathbf{u}^{n+1}) \\ &\quad=\frac{1}{2}\Big(\|\mathbf{u}^{n+1}\|^2-\|\mathbf{u}^{n}\|^2+\|2\mathbf{u}^{n+1}-\mathbf{u}^{n}\|^2-\|2\mathbf{u}^{n}-\mathbf{u}^{n-1}\|^2 \\ &\qquad+\|\mathbf{u}^{n+1}-2\mathbf{u}^{n}+\mathbf{u}^{n-1}\|^2\Big)+3(\|\tilde{\mathbf{u}}^{n+1}\|^2-\|\mathbf{u}^{n+1}\|^2), \end{aligned} \tag{3.34}$$

where we use the following identity

$$2(3a-4b+c,a)=a^2-b^2+(2a-b)^2-(2b-c)^2+(a-2b+c)^2. \tag{3.35}$$

We reformulate the projection step (3.24) as

$$\frac{3}{2\delta t}\mathbf{u}^{n+1}+\nabla p^{n+1}=\frac{3}{2\delta t}\tilde{\mathbf{u}}^{n+1}+\nabla p^{n}. \tag{3.36}$$

By taking the square of both sides of the above equation, we get

$$\frac{9}{4\delta t^2}\|\mathbf{u}^{n+1}\|^2+\|\nabla p^{n+1}\|^2=\frac{9}{4\delta t^2}\|\tilde{\mathbf{u}}^{n+1}\|^2+\|\nabla p^{n}\|^2+\frac{3}{\delta t}(\tilde{\mathbf{u}}^{n+1},\nabla p^{n}). \tag{3.37}$$

Hence, by multiplying $2\delta t^2/3$ of the above equation, we derive

$$\frac{3}{2}(\|\mathbf{u}^{n+1}\|^2-\|\tilde{\mathbf{u}}^{n+1}\|^2)+\frac{2\delta t^2}{3}(\|\nabla p^{n+1}\|^2-\|\nabla p^{n}\|^2)=2\delta t(\tilde{\mathbf{u}}^{n+1},\nabla p^{n}). \tag{3.38}$$

By taking the inner product of (3.24) with $2\delta t\mathbf{u}^{n+1}$ in the L^2 space, we have

$$\frac{3}{2}(\|\mathbf{u}^{n+1}\|^2-\|\tilde{\mathbf{u}}^{n+1}\|^2+\|\mathbf{u}^{n+1}-\tilde{\mathbf{u}}^{n+1}\|^2)=0. \tag{3.39}$$

We combine (3.32), (3.34), (3.38), and (3.39) to obtain

$$\begin{aligned} &\frac{1}{2}(\|\mathbf{u}^{n+1}\|^2-\|\mathbf{u}^{n}\|^2+\|2\mathbf{u}^{n+1}-\mathbf{u}^{n}\|^2-\|2\mathbf{u}^{n}-\mathbf{u}^{n-1}\|^2+\|\mathbf{u}^{n+1}-2\mathbf{u}^{n}+\mathbf{u}^{n-1}\|^2) \\ &\quad+\frac{3}{2}\|\mathbf{u}^{n+1}-\tilde{\mathbf{u}}^{n+1}\|^2+\frac{2\delta t^2}{3}(\|\nabla p^{n+1}\|^2-\|\nabla p^{n}\|^2)+2\delta t\|\sqrt{\nu}\nabla\tilde{\mathbf{u}}^{n+1}\|^2 \\ &\quad+2\delta t\,Q^{n+1}\left(\int_\Omega(\mathbf{u}^*\cdot\nabla)\mathbf{u}^*\cdot\tilde{\mathbf{u}}^{n+1}d\boldsymbol{x}+\int_\Omega(\phi^*\nabla\mu^*)\cdot\tilde{\mathbf{u}}^{n+1}d\boldsymbol{x}\right)=0. \end{aligned} \tag{3.40}$$

By taking the L^2 inner product of (3.19) with $2\delta t\mu^{n+1}$ in the L^2 space, we have

$$\begin{aligned}(3\phi^{n+1}-4\phi^n+\phi^{n-1},\mu^{n+1})+2\delta t\,Q^{n+1}\int_\Omega\nabla\cdot(\mathbf{u}^*\phi^*)\mu^{n+1}d\boldsymbol{x}\\ +\,2\delta t M\Big\|\mu^{n+1}-\frac{1}{|\Omega|}\int_\Omega\mu^{n+1}d\boldsymbol{x}\Big\|^2=0.\end{aligned}\tag{3.41}$$

By taking the L^2 inner product of (3.20) with $-(3\phi^{n+1}-4\phi^n+\phi^{n-1})$, we find

$$\begin{aligned}-(\mu^{n+1},3\phi^{n+1}-4\phi^n+\phi^{n-1})+\lambda(\nabla\phi^{n+1},\nabla(3\phi^{n+1}-4\phi^n+\phi^{n-1}))\\ +\,\lambda U^{n+1}\int_\Omega H^*(3\phi^{n+1}-4\phi^n+\phi^{n-1})d\boldsymbol{x}+\lambda\frac{s}{\epsilon^2}(\phi^{n+1},3\phi^{n+1}-4\phi^n+\phi^{n-1})=0.\end{aligned}\tag{3.42}$$

By taking the L^2 inner product of (3.21) with $2\lambda U^{n+1}$ and using (3.35), we obtain

$$\begin{aligned}\lambda\Big(|U^{n+1}|^2-|U^n|^2+|2U^{n+1}-U^n|^2-|2U^n-U^{n-1}|^2\\ +\,|U^{n+1}-2U^n+U^{n-1}|^2\Big)=\lambda U^{n+1}\int_\Omega H^*(3\phi^{n+1}-4\phi^n+\phi^{n-1})d\boldsymbol{x}.\end{aligned}\tag{3.43}$$

By multiplying (3.23) with $2\delta t\,Q^{n+1}$ and using (3.35), we obtain

$$\begin{aligned}\frac{1}{2}\Big(|Q^{n+1}|^2-|Q^n|^2+|2Q^{n+1}-Q^n|^2-|2Q^n-Q^{n-1}|^2+|Q^{n+1}-2Q^n+Q^{n-1}|^2\Big)\\ =2\delta t\,Q^{n+1}\int_\Omega\Big(\nabla\cdot(\mathbf{u}^*\phi^*)\mu^{n+1}+(\phi^*\nabla\mu^*)\cdot\tilde{\mathbf{u}}^{n+1}+(\mathbf{u}^*\cdot\nabla)\mathbf{u}^*\cdot\tilde{\mathbf{u}}^{n+1}\Big)d\boldsymbol{x}.\end{aligned}\tag{3.44}$$

Hence, by combining (3.40)–(3.44), we arrive at

$$\begin{aligned}&\frac{1}{2}(\|\mathbf{u}^{n+1}\|^2-\|\mathbf{u}^n\|^2+\|2\mathbf{u}^{n+1}-\mathbf{u}^n\|^2-\|2\mathbf{u}^n-\mathbf{u}^{n-1}\|^2)+\frac{2\delta t^2}{3}(\|\nabla p^{n+1}\|^2-\|\nabla p^n\|^2)\\ &+\frac{\lambda}{2}(\|\nabla\phi^{n+1}\|^2-\|\nabla\phi^n\|^2+\|\nabla(2\phi^{n+1}-\phi^n)\|^2-\|\nabla(2\phi^n-\phi^{n-1})\|^2)\\ &+\lambda(|U^{n+1}|^2-|U^n|^2+|2U^{n+1}-U^n|^2-|2U^n-U^{n-1}|^2)\\ &+\frac{1}{2}(|Q^{n+1}|^2-|Q^n|^2+|2Q^{n+1}-Q^n|^2-|2Q^n-Q^{n-1}|^2)\\ &+\frac{\lambda s}{2\epsilon^2}(\|\phi^{n+1}\|^2-\|\phi^n\|^2+\|2\phi^{n+1}-\phi^n\|^2-\|2\phi^n-\phi^{n-1}\|^2)\\ &+\Big\{\frac{1}{2}\|\mathbf{u}^{n+1}-2\mathbf{u}^n+\mathbf{u}^{n-1}\|^2+\frac{3}{2}\|\mathbf{u}^{n+1}-\tilde{\mathbf{u}}^{n+1}\|^2\\ &\quad+\frac{\lambda}{2}\|\nabla(\phi^{n+1}-2\phi^n+\phi^{n-1})\|^2+\frac{\lambda s}{2\epsilon^2}\|\phi^{n+1}-2\phi^n+\phi^{n-1}\|^2\\ &\quad+\lambda|U^{n+1}-2U^n+U^{n-1}|^2+\frac{1}{2}|Q^{n+1}-2Q^n+Q^{n-1}|^2\Big\}\\ &=-2\delta t\|\sqrt{\nu}\nabla\tilde{\mathbf{u}}^{n+1}\|^2-2\delta tM\Big\|\mu^{n+1}-\frac{1}{|\Omega|}\int_\Omega\mu^{n+1}d\boldsymbol{x}\Big\|^2.\end{aligned}\tag{3.45}$$

Finally, we obtain (3.30) after dropping the positive terms of (3.45) in { }. □

Remark 3.6. For the sake of completeness, here we present the commonly used temporal discretization methods for the nonlinearly coupled *adv-surf* terms, see also in [23,29,35,52,55,76–79]. For simplicity, we only discretize the related terms while other terms remain unchanged continuously so that readers can understand them more clearly. These schemes read as

$$\begin{cases}\phi_t+\underbrace{\nabla\cdot(\mathbf{u}^{n+1}\phi^n)}_{\text{Exp-Imp method}}+M\left(\mu^{n+1}-\dfrac{1}{|\Omega|}\displaystyle\int_\Omega\mu^{n+1}d\boldsymbol{x}\right)=0,\\ \dfrac{\mathbf{u}^{n+1}-\mathbf{u}^n}{\delta t}+(\mathbf{u}\cdot\nabla)\mathbf{u}-\nu\Delta\mathbf{u}+\nabla p+\underbrace{\phi^n\nabla\mu^{n+1}}_{\text{Exp-Imp method}}=0,\end{cases}\tag{3.46}$$

or

$$\begin{cases} \phi_t + \underbrace{\nabla\cdot(\mathbf{u}^{n+1}\phi^{n+1})}_{\text{Implicit method}} + M\left(\mu^{n+1} - \dfrac{1}{|\Omega|}\displaystyle\int_\Omega \mu^{n+1} d\boldsymbol{x}\right) = 0, \\ \dfrac{\mathbf{u}^{n+1}-\mathbf{u}^n}{\delta t} + (\mathbf{u}\cdot\nabla)\mathbf{u} - \nu\Delta\mathbf{u} + \nabla p + \underbrace{\phi^{n+1}\nabla\mu^{n+1}}_{\text{Implicit method}} = 0, \end{cases} \tag{3.47}$$

or

$$\begin{cases} \phi_t + \nabla\cdot((\mathbf{u}^n \underbrace{-\delta t\phi^n\nabla\mu^{n+1}}_{\text{Stab-method}})\phi^n) + M\left(\mu^{n+1} - \dfrac{1}{|\Omega|}\displaystyle\int_\Omega \mu^{n+1} d\boldsymbol{x}\right) = 0, \\ \dfrac{\mathbf{u}^{n+1}-\mathbf{u}^n}{\delta t} + (\mathbf{u}\cdot\nabla)\mathbf{u} - \nu\Delta\mathbf{u} + \nabla p + \underbrace{\phi^n\nabla\mu^{n+1}}_{\text{explicit since } \mu^{n+1} \text{ is obtained above}} = 0. \end{cases} \tag{3.48}$$

We can see that the scheme (3.46) is a coupled linear scheme because the *adv-surf* terms are handled by the Exp–Imp method; the scheme (3.47) is a coupled nonlinear scheme because the *adv-surf* terms are implicitly processed; and the scheme (3.48) is a fully-decoupled and linear scheme developed by the Stab-method, but the extra stabilization term $(-\delta t\phi^n\nabla\mu^{n+1})$ added in the advection contains the implicit processed potential μ^{n+1}, so it is necessary to solve the phase-field equation with variable coefficients at each time step. In addition, (3.46) and (3.47) have a second-order time-accurate version, while (3.48) only has a first-order version so far.

Compared with the above schemes that either have a coupling structure, or variable coefficients, or only have first-order time accuracy, the scheme (3.19)–(3.25) developed in this article is linear, fully-decoupled, second-order time-accurate, and unconditionally energy stable, which illustrates very high efficiency in practice.

3.2. D-CAC model

Now we develop the numerical scheme to solve the D-CAC model (2.15)–(2.18). Since the nonlinear coupling terms in the D-CAC model are the same as that in the NS-CAC model, we ignore the duplication steps for simplicity.

3.2.1. Reformulation

We still introduce a nonlocal variable $Q(t)$ and an ODE system related to it that reads as:

$$\begin{cases} Q_t = \displaystyle\int_\Omega (\nabla\cdot(\mathbf{u}\phi)\mu + (\phi\nabla\mu)\cdot\mathbf{u})\, d\boldsymbol{x}, \\ Q|_{(t=0)} = 1, \\ \mathbf{u}\cdot\mathbf{n}|_{\partial\Omega} = 0, \text{ or all variables are periodic.} \end{cases} \tag{3.49}$$

The ODE (3.49) is still equivalent to a trivial ODE ($Q_t = 0$, $Q|_{(t=0)} = 1$) which has the solution of $Q(t) = 1$. The other nonlocal variable U is still defined as (3.2). Then, by using the two variables Q, U, and combining the ODE (3.49), the D-CAC system (2.15)–(2.18) is reformulated to the following equivalent form:

$$\phi_t + Q\nabla\cdot(\mathbf{u}\phi) = -M\left(\mu - \frac{1}{|\Omega|}\int_\Omega \mu d\boldsymbol{x}\right), \tag{3.50}$$

$$\mu = \lambda(-\Delta\phi + \frac{s}{\epsilon^2}\phi + HU), \tag{3.51}$$

$$U_t = \frac{1}{2}\int_\Omega H\phi_t d\boldsymbol{x}, \tag{3.52}$$

$$\tau\mathbf{u}_t + \alpha\nu\mathbf{u} + \nabla p + Q\phi\nabla\mu = 0, \tag{3.53}$$

$$\nabla\cdot\mathbf{u} = 0, \tag{3.54}$$

$$Q_t = \int_\Omega \Big(\nabla\cdot(\mathbf{u}\phi)\mu + (\phi\nabla\mu)\cdot\mathbf{u}\Big) d\boldsymbol{x}, \tag{3.55}$$

where $H(\phi)=\frac{f(\phi)-\frac{s}{\epsilon^2}\phi}{\sqrt{\int_\Omega(F(\phi)-\frac{s}{2\epsilon^2}\phi^2)d\boldsymbol{x}+B}}$. The initial conditions read as

$$\begin{aligned}&\mathbf{u}|_{(t=0)}=\mathbf{u}^0,\ p|_{(t=0)}=p^0,\ \phi|_{(t=0)}=\phi^0,\\&Q|_{(t=0)}=1,\ U|_{(t=0)}=\sqrt{\int_\Omega(F(\phi^0)-\frac{s}{2\epsilon^2}(\phi^0)^2)d\boldsymbol{x}+B}.\end{aligned}\tag{3.56}$$

and the boundary conditions are either periodic or

$$\mathbf{u}\cdot\mathbf{n}|_{\partial\Omega}=0,\ \partial_{\mathbf{n}}\phi|_{\partial\Omega}=0.\tag{3.57}$$

3.2.2. Decoupled scheme for the d-CAC model

Similar to the scheme (3.19)–(3.25) for the NS-CAC model, we develop the BDF2 scheme to solve the equivalent D-CAC model (3.50)–(3.55) as follows. We update $(\tilde{\mathbf{u}},\mathbf{u},p,\phi,\mu,Q,U)^{n+1}$ by

$$\frac{a\phi^{n+1}-b\phi^n+c\phi^{n-1}}{2\delta t}+Q^{n+1}\nabla\cdot(\mathbf{u}^*\phi^*)=-M\left(\mu^{n+1}-\frac{1}{|\Omega|}\int_\Omega\mu^{n+1}d\boldsymbol{x}\right),\tag{3.58}$$

$$\mu^{n+1}=\lambda(-\Delta\phi^{n+1}+\frac{s}{\epsilon^2}\phi^{n+1}+H^*U^{n+1}),\tag{3.59}$$

$$aU^{n+1}-bU^n+cU^{n-1}=\frac{1}{2}\int_\Omega H^*(3\phi^{n+1}-4\phi^n+\phi^{n-1})d\boldsymbol{x},\tag{3.60}$$

$$\tau\frac{a\tilde{\mathbf{u}}^{n+1}-b\mathbf{u}^n+c\mathbf{u}^{n-1}}{2\delta t}+\alpha\nu\tilde{\mathbf{u}}^{n+1}+\nabla p^n+Q^{n+1}\phi^*\nabla\mu^*=0,\tag{3.61}$$

$$\frac{aQ^{n+1}-bQ^n+cQ^{n-1}}{2\delta t}=\int_\Omega\Big(\nabla\cdot(\mathbf{u}^*\phi^*)\mu^{n+1}+(\phi^*\nabla\mu^*)\cdot\tilde{\mathbf{u}}^{n+1}\Big)d\boldsymbol{x},\tag{3.62}$$

and

$$\tau\frac{a}{2\delta t}(\mathbf{u}^{n+1}-\tilde{\mathbf{u}}^{n+1})+\nabla(p^{n+1}-p^n)=0,\tag{3.63}$$

$$\nabla\cdot\mathbf{u}^{n+1}=0,\tag{3.64}$$

where the boundary conditions are either periodic or the following

$$\mathbf{u}^{n+1}\cdot\mathbf{n}|_{\partial\Omega}=\partial_{\mathbf{n}}\phi^{n+1}|_{\partial\Omega}=0.\tag{3.65}$$

We give the details on how to obtain the decoupling structure and implementation details, see Appendix A.2.

Remark 3.7. For the sake of completeness, here we present the fully-decoupled scheme developed in [23] applied to the D-CAC model. We know that method in [23] deals with the Darcy coupled Cahn–Hilliard model, so we just apply its decoupling method to the Darcy coupled CAC model. For simplicity, only the first-order version is given here, since the second-order version follows the same line. The scheme in [23] reads as

$$\phi_t+\nabla\cdot(\mathbf{u}^{n+1}\phi^n)+M\left(\mu^{n+1}-\frac{1}{|\Omega|}\int_\Omega\mu^{n+1}d\boldsymbol{x}\right)=0,\tag{3.66}$$

$$\tau\frac{\mathbf{u}^{n+1}-\mathbf{u}^n}{\delta t}+\alpha\nu\mathbf{u}^{n+1}+\nabla p^n+\phi^n\nabla\mu^{n+1}=0.\tag{3.67}$$

Note that the *adv-surf* terms are just discretized using the traditional Exp–Imp method, similar to (3.46). Due to the special format of the Darcy equations, by using the explicit linear relationship between $\mathbf{u}^{n+1}$ and other items, the decoupling structure of the above scheme can be obtained. More precisely, one can rewrite (3.67) as

$$\mathbf{u}^{n+1}=\frac{1}{\frac{\tau}{\delta t}+\alpha\nu}\Big(\frac{\tau}{\delta t}\mathbf{u}^n-\nabla p^n+\phi^n\nabla\mu^{n+1}\Big).\tag{3.68}$$

Then, the scheme (3.66) can be reformulated as

$$\phi_t+\frac{1}{\frac{\tau}{\delta t}+\alpha\nu}\nabla\cdot\Big((\frac{\tau}{\delta t}\mathbf{u}^n-\nabla p^n+\phi^n\nabla\mu^{n+1})\phi^n\Big)+M\left(\mu^{n+1}-\frac{1}{|\Omega|}\int_\Omega\mu^{n+1}d\boldsymbol{x}\right)=0.\tag{3.69}$$

This scheme does achieve a full decoupling structure, however, it is necessary to solve the phase-field equation with variable coefficients (for μ^{n+1}) at each time step, which increases the practical computational cost (as shown in Fig. 4.3).

3.2.3. Unconditional energy stability

Now we prove that the scheme (3.58)–(3.64) is unconditionally energy stable as follows.

Theorem 3.2. *The time-discrete scheme (3.58)–(3.64) satisfies the discrete energy dissipation law as follows*

$$\frac{1}{\delta t}(E^{n+1}-E^{n-1}) \le -\alpha\|\sqrt{\nu}\tilde{\mathbf{u}}^{n+1}\|^2 - M\left\|\mu^{n+1}-\frac{1}{|\Omega|}\int_\Omega \mu^{n+1}d\boldsymbol{x}\right\|^2 \le 0, \tag{3.70}$$

where

$$\begin{aligned} E^{n+1} =& \frac{\tau}{2}\Big(\frac{1}{2}\|\mathbf{u}^{n+1}\|^2+\frac{1}{2}\|2\mathbf{u}^{n+1}-\mathbf{u}^n\|^2\Big)+\frac{\delta t^2}{3\tau}\|\nabla p^{n+1}\|^2 \\ &+\frac{\lambda}{2}\Big(\frac{1}{2}\|\nabla\phi^{n+1}\|^2+\frac{1}{2}\|2\nabla\phi^{n+1}-\nabla\phi^n\|^2\Big) \\ &+\frac{\lambda s}{2\epsilon^2}\Big(\frac{1}{2}\|\phi^{n+1}\|^2+\frac{1}{2}\|2\phi^{n+1}-\phi^n\|^2\Big) \\ &+\lambda\Big(\frac{1}{2}|U^{n+1}|^2+\frac{1}{2}|2U^{n+1}-U^n|^2\Big)+\frac{1}{2}\Big(\frac{1}{2}|Q^{n+1}|^2+\frac{1}{2}|2Q^{n+1}-Q^n|^2\Big). \end{aligned} \tag{3.71}$$

Proof. After taking the inner product of (3.61) with $2\delta t\tilde{\mathbf{u}}^{n+1}$ in the L^2 space, we arrive at the following equation:

$$\begin{aligned} &\tau(3\tilde{\mathbf{u}}^{n+1}-4\mathbf{u}^n+\mathbf{u}^{n-1},\tilde{\mathbf{u}}^{n+1})+\alpha\delta t\|\sqrt{\nu}\tilde{\mathbf{u}}^{n+1}\|^2+2\delta t(\nabla p^n,\tilde{\mathbf{u}}^{n+1}) \\ &\quad+2\delta t\,Q^{n+1}\int_\Omega \phi^*\nabla\mu^*\cdot\tilde{\mathbf{u}}^{n+1}d\boldsymbol{x}=0. \end{aligned} \tag{3.72}$$

Since the schemes (3.63)–(3.64) are the same as (3.24)–(3.25), by taking the same process as the proof in Theorem 3.1, we can also obtain (3.34), (3.38), and (3.39). Therefore, by combining them with (3.72), we obtain

$$\begin{aligned} &\frac{\tau}{2}(\|\mathbf{u}^{n+1}\|^2-\|\mathbf{u}^n\|^2+\|2\mathbf{u}^{n+1}-\mathbf{u}^n\|^2-\|2\mathbf{u}^n-\mathbf{u}^{n-1}\|^2+\|\mathbf{u}^{n+1}-2\mathbf{u}^n+\mathbf{u}^{n-1}\|^2) \\ &\quad+\frac{3\tau}{2}\|\mathbf{u}^{n+1}-\tilde{\mathbf{u}}^{n+1}\|^2+\frac{2\delta t^2}{3\tau}(\|\nabla p^{n+1}\|^2-\|\nabla p^n\|^2)+2\alpha\delta t\|\sqrt{\nu}\tilde{\mathbf{u}}^{n+1}\|^2 \\ &\quad+2\delta t\,Q^{n+1}\int_\Omega\phi^*\nabla\mu^*\cdot\tilde{\mathbf{u}}^{n+1}d\boldsymbol{x}=0. \end{aligned} \tag{3.73}$$

By taking the L^2 inner product of (3.58) with $2\delta t\mu^{n+1}$ in the L^2 space, we have

$$\begin{aligned} &(3\phi^{n+1}-4\phi^n+\phi^{n-1},\mu^{n+1})+2\delta t\,Q^{n+1}\int_\Omega\nabla\cdot(\mathbf{u}^*\phi^*)\mu^{n+1}d\boldsymbol{x} \\ &\quad+2\delta t M\left\|\mu^{n+1}-\frac{1}{|\Omega|}\int_\Omega\mu^{n+1}d\boldsymbol{x}\right\|^2=0. \end{aligned} \tag{3.74}$$

By taking the L^2 inner product of (3.59) with $-(3\phi^{n+1}-4\phi^n+\phi^{n-1})$, we find

$$\begin{aligned} &-(\mu^{n+1},3\phi^{n+1}-4\phi^n+\phi^{n-1})+\lambda(\nabla\phi^{n+1},\nabla(3\phi^{n+1}-4\phi^n+\phi^{n-1})) \\ &\quad+\lambda U^{n+1}\int_\Omega H^*(3\phi^{n+1}-4\phi^n+\phi^{n-1})dbx \\ &\quad+\lambda\frac{s}{\epsilon^2}(\phi^{n+1},3\phi^{n+1}-4\phi^n+\phi^{n-1})=0. \end{aligned} \tag{3.75}$$

By taking the L^2 inner product of (3.60) with $2\lambda U^{n+1}$ and using (3.35), we obtain

$$\begin{aligned} &\lambda\Big(|U^{n+1}|^2-|U^n|^2+|2U^{n+1}-U^n|^2-|2U^n-U^{n-1}|^2 \\ &\quad+|U^{n+1}-2U^n+U^{n-1}|^2\Big)=\lambda U^{n+1}\int_\Omega H^*(3\phi^{n+1}-4\phi^n+\phi^{n-1})d\boldsymbol{x}. \end{aligned} \tag{3.76}$$

By multiplying (3.62) with $2\delta t\, Q^{n+1}$ and using (3.35), we obtain

$$\begin{aligned}\frac{1}{2}\Big(\,|Q^{n+1}|^2-|Q^n|^2+|2Q^{n+1}-Q^n|^2-|2Q^n-Q^{n-1}|^2+|Q^{n+1}-2Q^n+Q^{n-1}|^2\,\Big)\\ =2\delta t\, Q^{n+1}\int_\Omega\Big(\nabla\cdot(\mathbf{u}^*\phi^*)\mu^{n+1}+(\phi^*\nabla\mu^*)\cdot\tilde{\mathbf{u}}^{n+1}\Big)d\boldsymbol{x}.\end{aligned}\tag{3.77}$$

Hence, by combining (3.73)–(3.77), we arrive at

$$\begin{aligned}&\frac{\tau}{2}(\|\mathbf{u}^{n+1}\|^2-\|\mathbf{u}^n\|^2+\|2\mathbf{u}^{n+1}-\mathbf{u}^n\|^2-\|2\mathbf{u}^n-\mathbf{u}^{n-1}\|^2)+\frac{2\delta t^2}{3\tau}(\|\nabla p^{n+1}\|^2-\|\nabla p^n\|^2)\\ &\quad+\frac{\lambda}{2}(\|\nabla\phi^{n+1}\|^2-\|\nabla\phi^n\|^2+\|\nabla(2\phi^{n+1}-\phi^n)\|^2-\|\nabla(2\phi^n-\phi^{n-1})\|^2)\\ &\quad+\lambda(|U^{n+1}|^2-|U^n|^2+|2U^{n+1}-U^n|^2-|2U^n-U^{n-1}|^2)\\ &\quad+\frac{1}{2}(|Q^{n+1}|^2-|Q^n|^2+|2Q^{n+1}-Q^n|^2-|2Q^n-Q^{n-1}|^2)\\ &\quad+\frac{\lambda s}{2\epsilon^2}(\|\phi^{n+1}\|^2-\|\phi^n\|^2+\|2\phi^{n+1}-\phi^n\|^2-\|2\phi^n-\phi^{n-1}\|^2)\\ &\quad+\Big\{\frac{\tau}{2}\|\mathbf{u}^{n+1}-2\mathbf{u}^n+\mathbf{u}^{n-1}\|^2+\frac{3\tau}{2}\|\mathbf{u}^{n+1}-\tilde{\mathbf{u}}^{n+1}\|^2\\ &\qquad+\frac{\lambda}{2}\|\nabla(\phi^{n+1}-2\phi^n+\phi^{n-1})\|^2+\frac{\lambda s}{2\epsilon^2}\|\phi^{n+1}-2\phi^n+\phi^{n-1}\|^2\\ &\qquad+\lambda|U^{n+1}-2U^n+U^{n-1}|^2+\frac{1}{2}|Q^{n+1}-2Q^n+Q^{n-1}|^2\Big\}\\ &=-2\alpha\delta t\|\sqrt{\nu}\tilde{\mathbf{u}}^{n+1}\|^2-2\delta t M\Big\|\mu^{n+1}-\frac{1}{|\Omega|}\int_\Omega\mu^{n+1}d\boldsymbol{x}\Big\|^2.\end{aligned}\tag{3.78}$$

Finally, we obtain (3.70) after dropping the positive terms of (3.78) in { }. □

4. Numerical simulations

In this section, we first verify the stability/accuracy of the proposed schemes (3.19)–(3.25) and (3.58)–(3.64). Then we implement several simulations, including the spinodal decompositions for the NS-CAC model and the fingering instability due to the continuous injection flow for the D-CAC model.

The computational domain is set to be a rectangular type with $(x, y) \in \Omega = [0, L_x] \times [0, L_y]$ for 2D, and $(x, y, z) \in \Omega = [0, L_x] \times [0, L_y] \times [0, L_z]$ for 3D. The Fourier spectral method is used to discretize the direction satisfying the periodic boundary conditions. The Legendre–Galerkin method (cf. [80]) is used to discretize the directions with physical boundary conditions given by (3.27) and (3.65), in which P_N is used for ϕ, μ, and the inf–sup stable pair (P_N, P_{N-2}) is used for the velocity field and pressure p, respectively,

4.1. Accuracy and stability

In this subsection, we implement numerical tests to verify the accuracy and energy stability of the schemes (3.19)–(3.25) for solving the NS-CAC model, (3.58)–(3.64) for solving the D-CAC model. For convenience, we abbreviate them as DSAV.

We set the 2D computational domain to be $\Omega = [0, 2\pi]^2$, and assume that the x-direction satisfies the periodic boundary condition. The physical boundary conditions (3.27) and (3.65) are assumed along the y-direction for the NS-CAC model and D-CAC model, respectively. We set the initial conditions to two circles with different radii that read as follows:

$$\begin{cases}\phi^0(x,y)=1+\displaystyle\sum_{i=1}^{2}\tanh\Big(\frac{r_i-\sqrt{(x-x_i)^2+(y-y_i)^2}}{1.5\epsilon}\Big),\\ \mathbf{u}^0(x,y)=\mathbf{0},\ p^0(x,y)=0,\end{cases}\tag{4.1}$$

where $r_1 = 1.4$, $r_2 = 0.5$, $x_1 = \pi - 0.8$, $x_2 = \pi + 1.7$, $y_1 = y_2 = \pi$. For the NS-CAC model, we set the model parameters as $\nu = 1$, $\lambda = 0.01$, $\epsilon = 0.05$, $M = 10$, $B = 10$, and $S = 2$. For the D-CAC model, we set the model

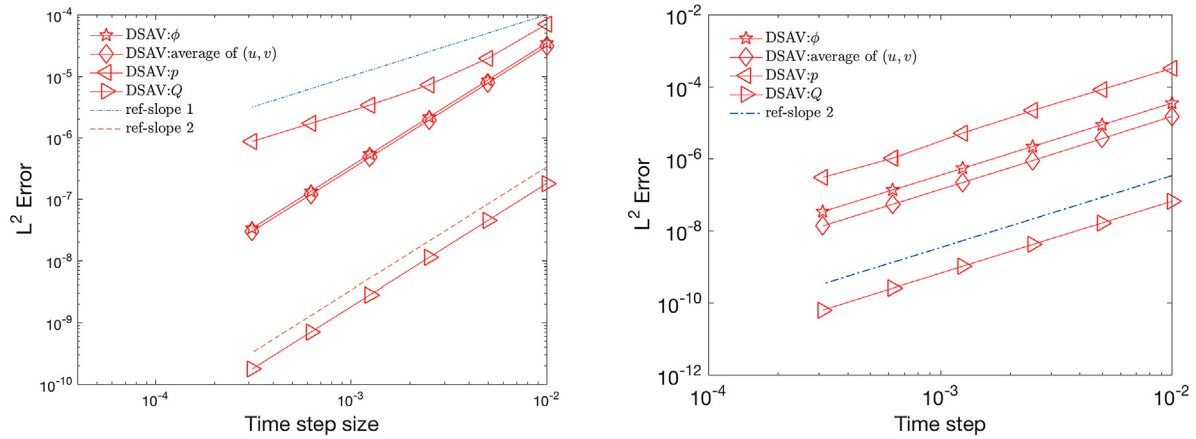

(a) DSAV scheme for NS-CAC model. (b) DSAV scheme for D-CAC model.

Fig. 4.1. Accuracy tests computed by the DSAV scheme where the L^2 numerical errors are plotted at $t = 0.2$ for the phase-field variable ϕ, the average of the two velocity components (u, v), the pressure p, and the auxiliary variable Q for (a) NS-CAC model and (b) D-CAC model.

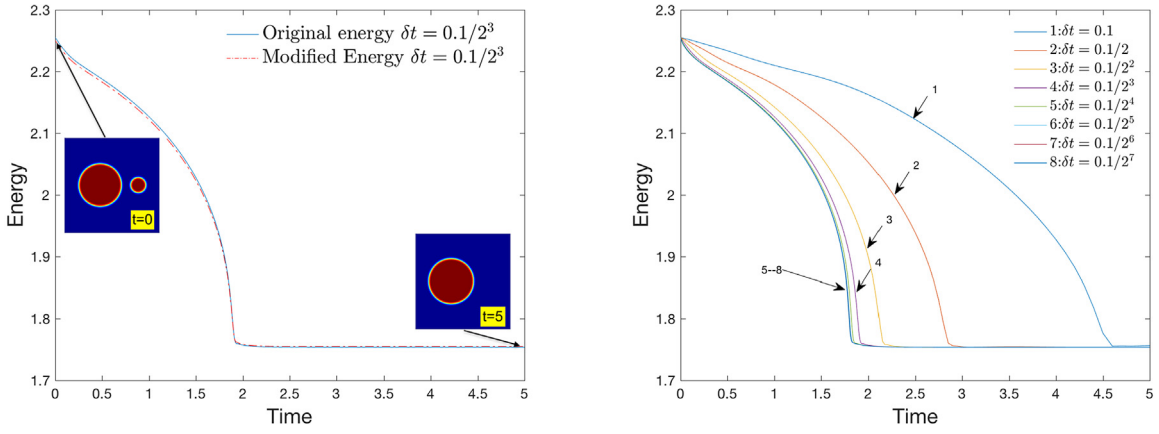

(a) Energy evolution using $\delta t = 0.1/2^3$. (b) Energy evolution with various δt.

Fig. 4.2. (a) The comparisons of the energy (2.2) in the original form and the energy (3.31) in the modified form computed by using the time step $\delta t = 0.1/2^3$, and (b) the evolutions of energy (2.2) computed with different δt.

parameters as $\alpha = 100$, $\nu = 1$, $\lambda = 0.01$, $\epsilon = 0.05$, $M = 10$, $B = 10$, and $S = 2$. We discretize the x-direction by using 257 Fourier modes and use Legendre polynomials with the degree up to 256 to discretize the y-direction. Using this sufficient fine grid, the interface can be well resolved, so that the spatial errors are negligible compared with the temporal errors. We use the numerical solutions calculated by using the scheme DSAV with a very tiny time step size $\delta t = 1\text{e}{-8}$ as the exact solutions.

In Fig. 4.1(a) and (b), for the DSAV schemes of the NS-CAC model and the D-CAC model, respectively, by using different time step sizes, we plot the numerical errors of L^2 at $t = 0.2$ between the obtained solutions and the exact solutions. We notice that for both models, the DSAV schemes provide second-order accuracy for the variables $(\phi, \mathbf{u}, Q)$. For the NS-CAC model, the pressure accuracy is first-order, and for the D-CAC model, the pressure accuracy is the second-order.

In Fig. 4.2(a), we show the difference between the original free energy (2.2) and the discrete energy (3.31) computed using the time step size $\delta t = 0.1/2^3$. We see that there is almost no visible difference between them. We also append the small inset figures for the phase-field ϕ at the initial moment and the steady-state where we can see that the small circle is finally absorbed into the big circle due to the coarsening effect.

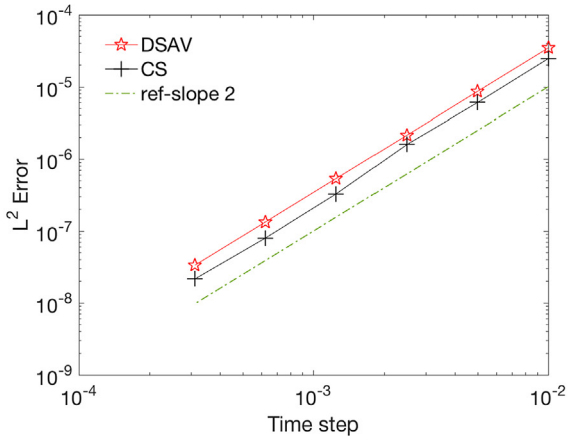

(a) Accuracy of DSAV and CS for ϕ.

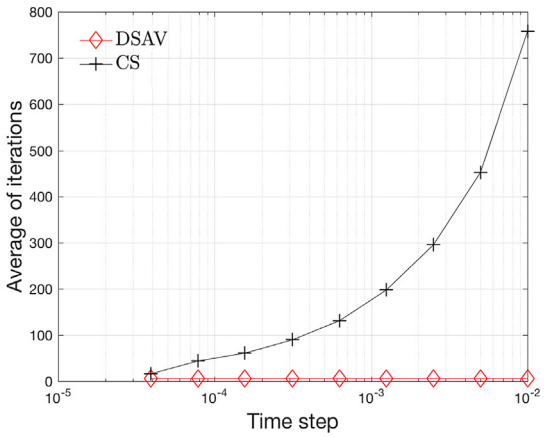

(b) Average number of iterations needed by DSAV and CS for each time step.

Fig. 4.3. The comparisons of L^2 errors for ϕ, and the average number of iterations needed by the scheme DSAV and scheme CS (developed in [23]) per time step for the D-CAC model.

Furthermore, we use different time steps to test the energy stability of the scheme DSAV. Since there is no visible difference between the original energy (2.2) and (3.31) shown in Fig. 4.2(a), in this test, we plot the evolution curves of the total free energy in the original form (2.2) calculated by DSAV using different time steps in Fig. 4.2(b) for the NS-CAC model. It can be seen that the obtained energy evolution curves always show monotonic decays, which means that DSAV is unconditionally energy stable. Moreover, as the time step gets smaller and smaller, the obtained energy curves overlap with each other, indicating that the obtained solution is getting closer and closer to the exact solution.

To show the effectiveness of the scheme DSAV, in Fig. 4.3, for the D-CAC model, we compare the scheme DSAV with another type of fully-decoupled scheme developed in [23] (see also Remark 3.7) where the convex-splitting scheme is used for the double-well potential and implicit–explicit combination method is used for the *adv-surf* terms (denoted by CS, for short). In Fig. 4.3(a), we compare the L^2 error obtained by DSAV and CS. For each δt, the error obtained by CS is slightly less than DSAV since the scheme CS handles many terms implicitly which can give better accuracy. However, if we further test the average number of iterations of these two schemes, as shown in Fig. 4.3(b), we immediately find the scheme DSAV is much more efficient than CS.

4.2. Spinodal decomposition

In this example, for the NS-CAC model, we investigate the spinodal decomposition (phase separation). The initial conditions are set as follows,

$$\mathbf{u}^0(\boldsymbol{x}) = \mathbf{0},\ p^0(\boldsymbol{x}) = 0,\ \phi(\boldsymbol{x}) = \bar{\phi}_0 + 0.001\text{rand}(\boldsymbol{x}), \tag{4.2}$$

where the rand($\boldsymbol{x}$) is the random number in $[-1, 1]$ that follows the normal distribution.

We perform 3D simulations and set the computational domain to be $\Omega = [0, 2\pi]^3$. We set the model parameters as $\nu = 1$, $\lambda = 0.01$, $\epsilon = 0.04$, $M = 100$, $B = 10$, $S = 2$, and set $\delta t = 5\text{e}{-4}$ for better accuracy. The periodic boundary conditions are assumed and the space is discretized using the Fourier-spectral method where 256^3 Fourier modes are adopted. We vary the initial average $\bar{\phi}_0$, and plot the steady-state contour in Fig. 4.4, where, to get a more accurate view, we plot the steady-state for the domain of $[0, 4\pi]^3$ (8 periods) for all simulated cases. The equilibrium solution presents the P-Schwarz surface phase ($\bar{\phi}_0 = 0$), Lamella phase ($\bar{\phi}_0 = 0.1$), Lawson surface phase ($\bar{\phi}_0 = 0.3, 0.35, 0.45$), cylindrical phase ($\bar{\phi}_0 = 0.4$), and spherical phase ($\bar{\phi}_0 = 0.55$). These simulations show qualitatively consistent features with the numerical/experimental results obtained in [81–83]. In Fig. 4.5, the total free energy functional (scaled by applying the logarithm function) (3.31) is plotted.

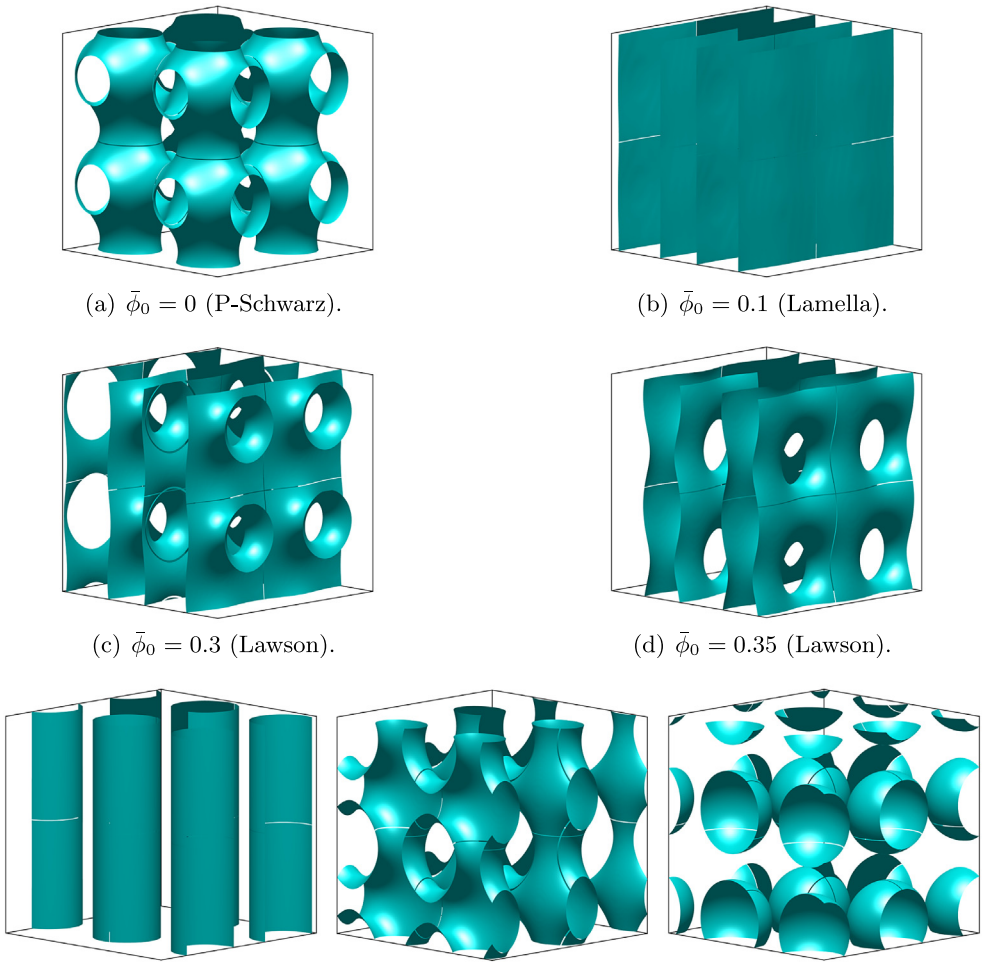

(a) $\bar{\phi}_0 = 0$ (P-Schwarz). (b) $\bar{\phi}_0 = 0.1$ (Lamella).

(c) $\bar{\phi}_0 = 0.3$ (Lawson). (d) $\bar{\phi}_0 = 0.35$ (Lawson).

(e) $\bar{\phi}_0 = 0.4$ (Cylindrical). (f) $\bar{\phi}_0 = 0.45$ (Lawson). (g) $\bar{\phi}_0 = 0.55$ (Spherical).

Fig. 4.4. The isosurfaces of $\{\phi = 0\}$ for eight periods $[0, 4\pi]^3$ for the equilibrium solutions of 3D spinodal decompositions example with $\bar{\phi}_0 = 0$, 0.1, 0.3, 0.35, 0.4, 0.45, and 0.55 for the NS-CAC model.

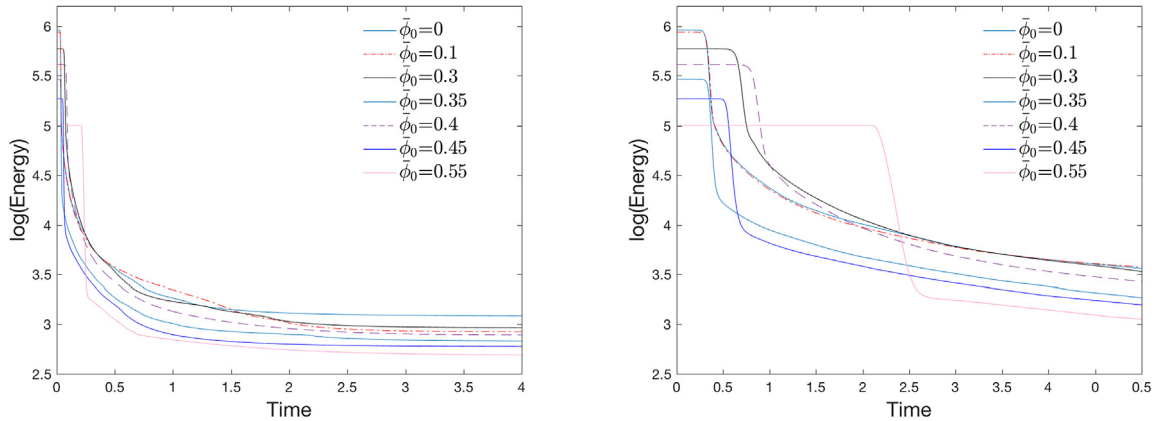

(a) Energy evolutions. (b) A close-up view.

Fig. 4.5. Time evolutions of the logarithm of total free energy (3.31) for all 3D spinodal decomposition examples with various initial values of $\bar{\phi}_0$.

4.3. Fingering instability of D-CAC model

In this subsection, using the D-CAC model, we simulate the viscous fingering pattern instability problem (Saffman–Taylor instability), which is one of the most in-depth studied research problems in fluid dynamic systems, which demonstrate the formation and evolution of elaborate patterned structures. It considers the development of interfacial instabilities when a fluid displaces another of higher viscosity between the narrowly spaced plates of a Hele–Shaw cell, see [84–86]. An extensively investigated version of the problem is the so-called radial fingering flow driven by injection. It considers the radial intrusion of a fluid of low-viscosity that is injected under a constant injection rate against a more viscous liquid that initially occupies the entire cell. Experiments involving the injection-driven radial flow for immiscible fluids show that as the size of the fluid–fluid interface grows outward, fingers form, spread out, and start to split at their tips, creating complex branched patterns [84–86].

We implement numerical simulations in 2D where $\Omega = [0, 2\pi]^2$ is the computed domain. To represent the injection flow, we adopt the Gaussian method designed in [85] where a potential radial velocity $\mathbf{u}_{pot}$ is imposed in the momentum equation and the phase-field equation, namely, the D-CAC model is revised as

$$\phi_t + \nabla \cdot ((\mathbf{u} + \mathbf{u}_{pot})\phi) + M\Big(\mu - \frac{1}{|\Omega|}\int_\Omega \mu d\boldsymbol{x}\Big) = 0, \tag{4.3}$$

$$\mu = \lambda(-\Delta\phi + f(\phi)), \tag{4.4}$$

$$\tau \mathbf{u}_t + \alpha\nu(\phi)(\mathbf{u} + \mathbf{u}_{pot}) + \nabla p + \phi\nabla\mu = 0, \tag{4.5}$$

$$\nabla \cdot \mathbf{u} = 0, \tag{4.6}$$

with

$$\begin{cases} \mathbf{u}_{pot}(x, y) = -C(1 - e^{-4r(x,y)^2/R_0^2})\tilde{\mathbf{r}}(x,y), \\ r(x, y) = \sqrt{(x-\pi)^2 + (y-\pi)^2}, \\ \tilde{\mathbf{r}}(x, y) = (\dfrac{x-\pi}{r(x,y)+\eta}, \dfrac{y-\pi}{r(x,y)+\eta}), \\ \nu(\phi) = \nu_1\dfrac{1-\phi}{2} + \nu_2\dfrac{1+\phi}{2}, \end{cases} \tag{4.7}$$

where C is the injection strength, R_0 is the radius of the circular injection region, η is a small quantity such that $r(x, y)+\eta \neq 0$ for any $(x, y) \in \Omega$, ν_1 is the viscosity of the displaced fluid, ν_2 is the viscosity of the injected fluid, and $\nu_1 > \nu_2$.

We set the initial conditions as follows:

$$\phi^0(x, y) = \tanh(\frac{\tilde{r} - \sqrt{(x-\pi)^2 - (y-\pi)^2}}{\epsilon}),\ \mathbf{u}^0(x, y) = (0, 0),\ p^0(x, y) = 0, \tag{4.8}$$

where $\tilde{r} = r_0 + 0.001(1 + \cos(k\theta))$ and $\theta = \arctan(\frac{y-\pi}{x-\pi})$ and k the wave number of the perturbation. We assume periodic boundary conditions and discretize the space by using the Fourier-spectral method, where each direction is discretized using 1025 Fourier modes. The model parameters read as

$$\begin{aligned} &r_0 = R_0 = 0.2, C = 25, \tau = 1, \alpha = 1000, \nu_1 = 20, \nu_2 = 1, \\ &M = 10, \epsilon = 0.008, \lambda = 0.01, B = 10, S = 2, \eta = 1\text{e}{-6}, \delta t = 1\text{e}{-5}. \end{aligned} \tag{4.9}$$

In Fig. 4.6(a)–(c), by using different wave numbers $k = 6, 14$ and 36, we plot the phase-field variable ϕ at different times (to be clearer, we use the grayscale snapshots). We observe that the droplet forms a clear fingering pattern over time. When the wave number increases, we can see a larger number of fingers forming, and on each finger, more bifurcations are formed.

Next, we test the effect of the viscosity of the displaced fluid on the formation of the fingering pattern. We set the model parameters as

$$\begin{aligned} &r_0 = R_0 = 0.8, k = 60, C = 25, \tau = 1, \alpha = 1000, \nu_2 = 1, \\ &M = 10, \epsilon = 0.008, \lambda = 0.01, B = 10, S = 2, \eta = 1\text{e}{-6}, \delta t = 1\text{e}{-5}. \end{aligned} \tag{4.10}$$

In Fig. 4.7, we plot the phase-field variable ϕ by varying the viscosity of the displaced fluid ν_1 such that it is increased from 2 to 200. When $\nu_1 = 2$, that is, the viscosity of the two fluids is very close, no fingering pattern

(a) $k = 6$ and snapshots are taken at $t = 0, 0.02, 0.04, 0.06, 0.08, 0.1$ and 0.12.

(b) $k = 14$ and snapshots are taken at $t = 0, 0.02, 0.04, 0.06, 0.08, 0.1$ and 0.13.

(c) $k = 36$ and snapshots are taken at $t = 0, 0.02, 0.04, 0.06, 0.08, 0.1$ and 0.12.

Fig. 4.6. Snapshots of the phase-field variable ϕ at different times which show the formation of fingering patterns where various wave numbers of the perturbation are used with (a) $k = 6$, (b) $k = 16$, and (c) $k = 36$. Blank and dark regions represent the injected fluid with less viscosity and the displaced fluid with higher viscosity, respectively.

is formed, shown in Fig. 4.7(a). With the increases of ν_1 that means the viscosity contrast becomes larger, while the number of main fingers remains roughly the same (see $t = 0.04$, the third subfigure in each of Fig. 4.7(b)–(e)), we can observe extremely complex patterns formed during the evolution of time. For example, the length of the branched fingers becomes uneven, some fingers grow up, become long, straight, or even bifurcated again; some fingers become short, bended, or even are pinched-off, as shown in Fig. 4.7(b)–(e) for $\nu_1 = 5, 20, 100, 200$, respectively.

5. Concluding remarks

In this article, for the two-phase flow model that couples the mass-conserved Allen–Cahn equation with two fluid flow systems (the incompressible Navier–Stokes equations and the Darcy equations), we develop a new full decoupling method, and combine it with other proven effective numerical methods, to form an efficient numerical scheme with full decoupling structure and second-order time accuracy. The scheme is highly efficient and only needs to solve linear elliptic equations with constant coefficients. The specialty of the new decoupling method is that by adding an additionally designed ODE to the PDE system, the nonlinear coupling term can be explicitly handled while still ensuring unconditional energy stability. We also conduct numerous numerical tests in 2D and 3D to demonstrate the accuracy and stability of the scheme.

Declaration of competing interest

The authors declare that they have no known competing financial interests or personal relationships that could have appeared to influence the work reported in this paper.

Acknowledgments

X. Yang was partially supported by USA National Science Foundation with grant numbers DMS-1720212, 1818783, and 2012490.

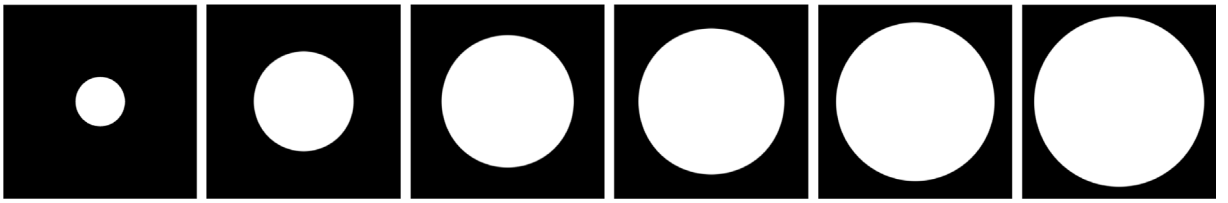

(a) $\nu_1 = 2$ and $t = 0, 0.04, 0.08, 0.1, 0.12, 0.14$.

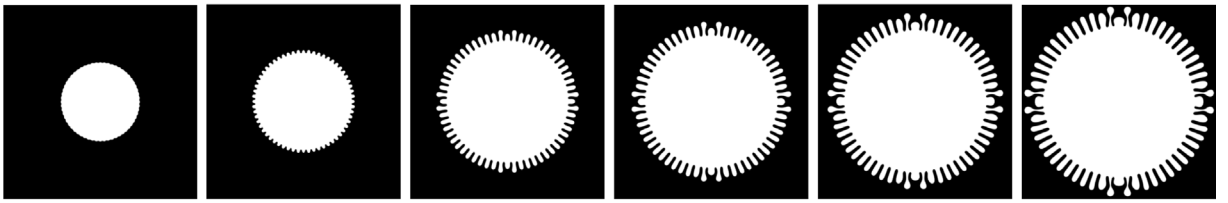

(b) $\nu_1 = 5$ and $t = 0.02, 0.04, 0.08, 0.1, 0.12, 0.14$.

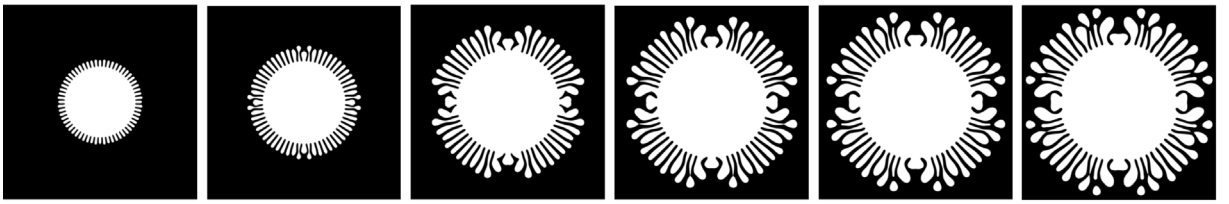

(c) $\nu_1 = 20$ and $t = 0.02, 0.04, 0.08, 0.1, 0.11, 0.12$.

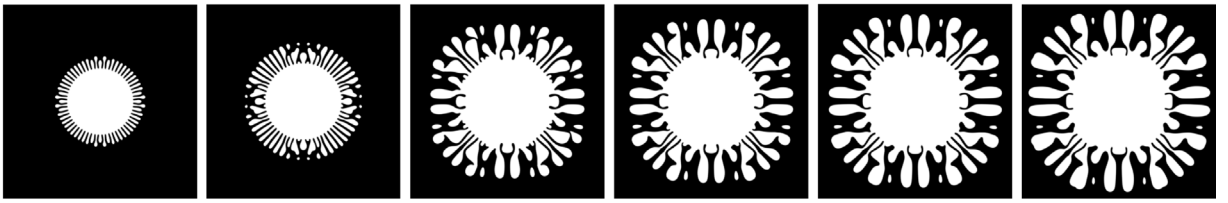

(d) $\nu_1 = 100$ and $t = 0.02, 0.04, 0.08, 0.09, 0.1, 0.11$.

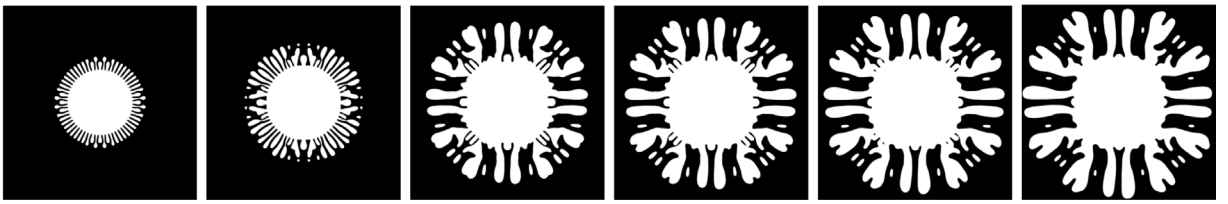

(e) $\nu_1 = 200$ and $t = 0.02, 0.04, 0.08, 0.09, 0.1, 0.11$.

Fig. 4.7. Snapshots of the phase-field variable ϕ at different times which show the formation of fingering patterns where the viscosity of displaced fluid ν_1 is varied with (a) $\nu_1 = 2$, (b) $\nu_1 = 5$, (c) $\nu_1 = 20$, (d) $\nu_1 = 100$, and (e) $\nu_1 = 200$. Blank and dark regions represent the injected fluid with less viscosity and the displaced fluid with higher viscosity, respectively.

Appendix. Decoupled implementation of schemes

A.1. Implementation of scheme (3.19)–(3.25)

We discuss how to obtain the decoupled structure of the scheme (3.19)–(3.25) where the key idea is the nonlocal property of the variable Q^{n+1}.

Step 1: we split $(\phi, \mu, U)^{n+1}$ into a linear combination form

$$\phi^{n+1} = \phi_1^{n+1} + Q^{n+1}\phi_2^{n+1}, \mu^{n+1} = \mu_1^{n+1} + Q^{n+1}\mu_2^{n+1}, U^{n+1} = U_1^{n+1} + Q^{n+1}U_2^{n+1}, \tag{A.1}$$

and solve $(\phi_1, \phi_2, \mu_1, \mu_2, U_1, U_2)^{n+1}$.

Using (A.1), the system (3.19)–(3.20) can be split into the following two subsystems:

$$\begin{cases} \dfrac{a}{2M\delta t}\phi_1^{n+1} = -\left(\mu_1^{n+1} - \dfrac{1}{|\Omega|}\displaystyle\int_\Omega \mu_1^{n+1}d\boldsymbol{x}\right) + \dfrac{b\phi^n - c\phi^{n-1}}{2M\delta t}, \\ \mu_1^{n+1} = \lambda\Big(-\Delta\phi_1^{n+1} + H^*U_1^{n+1} + \dfrac{s}{\epsilon^2}\phi_1^{n+1}\Big), \end{cases} \tag{A.2}$$

and

$$\begin{cases} \dfrac{a}{2M\delta t}\phi_2^{n+1} = -\left(\mu_2^{n+1} - \dfrac{1}{|\Omega|}\displaystyle\int_\Omega \mu_2^{n+1}d\boldsymbol{x}\right) - \dfrac{1}{M}\nabla\cdot(\mathbf{u}^*\phi^*), \\ \mu_2^{n+1} = \lambda\Big(-\Delta\phi_2^{n+1} + H^*U_2^{n+1} + \dfrac{s}{\epsilon^2}\phi_2^{n+1}\Big). \end{cases} \tag{A.3}$$

The boundary conditions described in (3.27) are requested to be periodic or satisfy

$$\partial_{\mathbf{n}}\phi_1^{n+1}|_{\partial\Omega} = \partial_{\mathbf{n}}\phi_2^{n+1}|_{\partial\Omega} = 0. \tag{A.4}$$

We consider the mass of ϕ_i^{n+1} and obtain it by taking the L^2 inner product with 1 for the first equation of (A.2) and the first equation of (A.3), and using Remark 3.3. Then we get

$$\int_\Omega \phi_1^{n+1}d\boldsymbol{x} = \int_\Omega \phi^n d\boldsymbol{x} = \int_\Omega \phi^{n-1}d\boldsymbol{x} = \int_\Omega \phi^0 d\boldsymbol{x}, \ \int_\Omega \phi_2^{n+1}d\boldsymbol{x} = 0, \tag{A.5}$$

which implies the ϕ_1^{n+1} maintain the total mass.

To solve $(\phi_1, \mu_1, \phi_2, \mu_2)^{n+1}$, we continue to split them using the two nonlocal variables U_1^{n+1} and U_2^{n+1} respectively, namely

$$\phi_i^{n+1} = \phi_{i1}^{n+1} + U_i^{n+1}\phi_{i2}^{n+1}, \mu_i^{n+1} = \mu_{i1}^{n+1} + U_i^{n+1}\mu_{i2}^{n+1}, i = 1, 2. \tag{A.6}$$

Replacing $(\phi_1, \phi_2, \mu_1, \mu_2)^{n+1}$ in the two subsystems (A.2) and (A.3) using (A.6), decomposing the obtained equations according to U_1^{n+1} and U_2^{n+1}, we get

$$\begin{cases} \dfrac{a}{2M\delta t}\phi_{ij}^{n+1} = -\left(\mu_{ij}^{n+1} - \dfrac{1}{|\Omega|}\displaystyle\int_\Omega \mu_{ij}^{n+1}d\boldsymbol{x}\right) + G_i, \\ \mu_{ij}^{n+1} = \lambda\Big(-\Delta\phi_{ij}^{n+1} + \dfrac{s}{\epsilon^2}\phi_{ij}^{n+1}\Big), i, j = 1, 2, \end{cases} \tag{A.7}$$

where $G_{11} = \frac{b\phi^n - c\phi^{n-1}}{2M\delta t}, G_{12} = G_{22} = 0, G_{21} = -\frac{1}{M}\nabla\cdot(\mathbf{u}^*\phi^*)$ and the boundary conditions are either $\partial_{\mathbf{n}}\phi_{ij}^{n+1}|_{\partial\Omega} = 0$ or periodic.

The mass of ϕ_{ij}^{n+1} can be obtained by taking the L^2 inner product with 1 for the first equation of the four subsystems of (A.7), that is

$$\begin{cases} \displaystyle\int_\Omega \phi_{11}^{n+1}d\boldsymbol{x} = \int_\Omega \phi^n d\boldsymbol{x} = \int_\Omega \phi^{n-1}d\boldsymbol{x} = \int_\Omega \phi^0 d\boldsymbol{x}, \\ \displaystyle\int_\Omega \phi_{12}^{n+1}d\boldsymbol{x} = \int_\Omega \phi_{21}^{n+1}d\boldsymbol{x} = \int_\Omega \phi_{22}^{n+1}d\boldsymbol{x} = 0. \end{cases} \tag{A.8}$$

To solve the four sub-systems (A.7), after combining the two equations in each sub-system together and using (A.8), we derive

$$\frac{a}{2M\delta t}\phi_{ij}^{n+1} + \lambda(-\Delta\phi_{ij}^{n+1} + \frac{s}{\epsilon^2}\phi_{ij}^{n+1}) = \hat{G}_{ij}, i, j = 1, 2, \tag{A.9}$$

where

$$\begin{cases} \hat{G}_{11} = \dfrac{b\phi^n - c\phi^{n-1}}{2M\delta t} + \lambda\dfrac{s}{\epsilon^2}\dfrac{1}{|\Omega|}\displaystyle\int_\Omega \phi_{11}^{n+1}d\boldsymbol{x}, \\ \hat{G}_{12} = \hat{G}_{22} = -\lambda(H^* - \dfrac{1}{|\Omega|}\displaystyle\int_\Omega H^* d\boldsymbol{x}), \hat{G}_{21} = -\dfrac{1}{M}\nabla\cdot(\mathbf{u}^*\phi^*). \end{cases} \tag{A.10}$$

It is very easy to solve (A.9) since all four equations are just elliptic equations with constant coefficients (note that $\phi_{12}^{n+1} = \phi_{22}^{n+1}$, thus we only need to solve three elliptic equations here).

Step 2: we further solve U^{n+1}. We rewrite (3.21) to be the following form:

$$U^{n+1} = \frac{1}{2}\int_\Omega H^*\phi^{n+1}d\boldsymbol{x} + g^n, \tag{A.11}$$

where $g^n = \frac{1}{3}(bU^n - cU^{n-1}) - \frac{1}{6}\int_\Omega H^*(b\phi^n - c\phi^{n-1})d\boldsymbol{x}$, and replace $(U,\phi)^{n+1}$ using (A.1) to get

$$U_1^{n+1} + Q^{n+1}U_2^{n+1} = \frac{1}{2}\int_\Omega H^*(\phi_1^{n+1} + Q^{n+1}\phi_2^{n+1})d\boldsymbol{x} + g^n. \tag{A.12}$$

According to Q^{n+1}, we get

$$U_i^{n+1} = \frac{1}{2}\int_\Omega H^*\phi_i^{n+1}d\boldsymbol{x} + G_u^i, i = 1,2, \tag{A.13}$$

where $G_u^1 = g^n$, $G_u^2 = 0$. We continue to replace $(\phi_1,\phi_2)^{n+1}$ in (A.13) using (A.6) and apply a simple factorization to derive

$$U_i^{n+1} = \frac{\frac{1}{2}\int_\Omega H^*\phi_{i1}^{n+1}d\boldsymbol{x} + G_u^i}{1 - \frac{1}{2}\int_\Omega H^*\phi_{i2}^{n+1}d\boldsymbol{x}}, i = 1,2, \tag{A.14}$$

We can directly solve $U_i^{n+1}, i = 1,2$ from (A.14) under the premise of (A.14) is always solvable. To show that, for the equation of $\phi_{i2}, i = 1,2$ in (A.9), by taking the L^2 inner product of them with ϕ_{i2}^{n+1} and using (A.8), we deduce

$$-\lambda\int_\Omega H^*\phi_{i2}^{n+1}d\boldsymbol{x} = \frac{a}{2M\delta t}\|\phi_{i2}^{n+1}\|^2 + \lambda\|\nabla\phi_{i2}^{n+1}\|^2 + \frac{\lambda s}{\epsilon^2}\|\phi_{i2}^{n+1}\|^2 \geq 0, i = 1,2. \tag{A.15}$$

Hence, the denominator in (A.14) is always non-zero which means it is always solvable. After $(U_1,U_2)^{n+1}$ are computed, $(\phi_1,\mu_1,\phi_2,\mu_2)^{n+1}$ can be updated from (A.6) directly.

Step 3: we solve the velocity field $\tilde{\mathbf{u}}^{n+1}$ in (3.22). We write $\tilde{\mathbf{u}}^{n+1}$ as

$$\tilde{\mathbf{u}}^{n+1} = \tilde{\mathbf{u}}_1^{n+1} + Q^{n+1}\tilde{\mathbf{u}}_2^{n+1}. \tag{A.16}$$

After replacing the variable $\tilde{\mathbf{u}}^{n+1}$ in (3.22) with (A.16), we split the obtained equation in terms of Q^{n+1} to obtain two sub-systems:

$$\frac{a}{2\delta t}\tilde{\mathbf{u}}_i^{n+1} - \nu\Delta\tilde{\mathbf{u}}_i^{n+1} = R_{\mathbf{u}}^i, i = 1,2, \tag{A.17}$$

where $R_{\mathbf{u}}^1 = -\nabla p^n + \frac{b\mathbf{u}^n - c\mathbf{u}^{n-1}}{2\delta t}$, $R_{\mathbf{u}}^2 = -(\mathbf{u}^*\cdot\nabla)\mathbf{u}^* - \phi^*\nabla\mu^*$. The boundary conditions of two variables $(\tilde{\mathbf{u}}_1,\tilde{\mathbf{u}}_2)^{n+1}$ are either periodic or satisfy $\tilde{\mathbf{u}}_1^{n+1}|_{\partial\Omega} = \tilde{\mathbf{u}}_2^{n+1}|_{\partial\Omega} = \mathbf{0}$. It is very easy to solve (A.17) since they are just elliptic equations with constant coefficients.

Step 4: we solve the auxiliary variable Q^{n+1}. Using the split form for the variables μ^{n+1}, $\tilde{\mathbf{u}}^{n+1}$, one can rewrite (3.23) as the following form:

$$(\frac{3}{2\delta t} - \eta_2)Q^{n+1} = \frac{1}{2\delta t}(4Q^n - Q^{n-1}) + \eta_1, \tag{A.18}$$

where

$$\eta_i = \int_\Omega\Big(\nabla\cdot(\mathbf{u}^*\phi^*)\mu_i^{n+1} + (\phi^*\nabla\mu^*)\cdot\tilde{\mathbf{u}}_i^{n+1} + (\mathbf{u}^*\cdot\nabla)\mathbf{u}^*\cdot\tilde{\mathbf{u}}_i^{n+1}\Big)d\boldsymbol{x}, i = 1,2. \tag{A.19}$$

It can be seen that the nonlocal equation (A.18) is very easy to be solved since η_1 and η_2 are all known terms obtained from Step 1–Step 3 under the premise of $\frac{3}{2\delta t} - \eta_2 \neq 0$. Once Q^{n+1} is computed from (A.18), we update $\tilde{\mathbf{u}}^{n+1}$ from (A.16), and $(\phi,\mu,U)^{n+1}$ from (A.1).

The premise of $\frac{3}{2\delta t} - \eta_2 \neq 0$ (solvability of (A.18)) can be obtained by performing the following simple energy estimates. By taking the L^2 inner product of the equation in (A.17) for $i = 2$ with $\tilde{\mathbf{u}}_2^{n+1}$, we deduce

$$-\int_\Omega\Big((\phi^*\nabla\mu^*)\cdot\tilde{\mathbf{u}}_2^{n+1} + (\mathbf{u}^*\cdot\nabla)\mathbf{u}^*\cdot\tilde{\mathbf{u}}_2^{n+1}\Big)d\boldsymbol{x} = \frac{a}{2\delta t}\|\tilde{\mathbf{u}}_2^{n+1}\|^2 + \|\sqrt{\nu}\nabla\tilde{\mathbf{u}}_2^{n+1}\|^2 \geq 0. \tag{A.20}$$

By taking the L^2 inner product of the first equation in (A.3) with μ_2^{n+1}, of the second equation in (A.3) with $-\frac{a}{2M\delta t}\phi_2^{n+1}$, and combining the two obtained equalities, we get

$$\begin{aligned}-\frac{1}{M}\int_\Omega \nabla\cdot(\mathbf{u}^*\phi^*)\mu_2^{n+1}d\boldsymbol{x} = &\left\|\mu_2^{n+1}-\frac{1}{|\Omega|}\int_\Omega \mu_2^{n+1}d\boldsymbol{x}\right\|^2\\ &+\frac{a\lambda}{2M\delta t}\|\nabla\phi_2^{n+1}\|^2+\frac{a\lambda s}{2M\delta t\epsilon^2}\|\phi_2^{n+1}\|^2\\ &+\frac{a\lambda}{2M\delta t}U_2^{n+1}\int_\Omega H^*\phi_2^{n+1}d\boldsymbol{x}.\end{aligned} \tag{A.21}$$

From (A.13) for $i=2$, we get $U_2^{n+1}\int_\Omega H^*\phi_2^{n+1}d\boldsymbol{x}=\frac{1}{2}(\int_\Omega H^*\phi_2^{n+1}d\boldsymbol{x})^2\geq 0$, which implies

$$-\int_\Omega \nabla\cdot(\mathbf{u}^*\phi^*)\mu_2^{n+1}d\boldsymbol{x}\geq 0. \tag{A.22}$$

From (A.20) and (A.22), we get $-\eta_2\geq 0$. Thus (A.18) is uniquely solvable.

Step 5: we update $\mathbf{u}^{n+1}$ and p^{n+1} from (3.24) and (3.25) using the method given in Remark 3.4.

The above implementation process shows that the calculation of all unknown variables can be completely decoupled. At each time step, the total cost of includes the solution of three linear elliptic equations of (A.9), two linear elliptic equations in (A.17), and one Poisson-type equation in step 5. The decoupling of all equations and the characteristic of having only constant coefficients means very efficient calculations in practice.

A.2. *Implementation of scheme* (3.58)–(3.64)

The implementation of the scheme (3.58)–(3.65) is also quite similar to the scheme (3.19)–(3.23) except Step 3. Hence we only give step 3 here.

Step 3: we split $\tilde{\mathbf{u}}^{n+1}$ using Q^{n+1} as:

$$\tilde{\mathbf{u}}^{n+1}=\tilde{\mathbf{u}}_1^{n+1}+Q^{n+1}\tilde{\mathbf{u}}_2^{n+1}. \tag{A.23}$$

We replace the variable $\tilde{\mathbf{u}}^{n+1}$ in (3.61) by using the split form given in (A.23), and then split the obtained equation in terms of Q^{n+1} to get

$$\begin{cases}\tau\dfrac{a}{2\delta t}\tilde{\mathbf{u}}_1^{n+1}+\alpha\nu\tilde{\mathbf{u}}_1^{n+1}=-\nabla p^n+\dfrac{b\mathbf{u}^n-c\mathbf{u}^{n-1}}{2\delta t},\\ \tau\dfrac{a}{2\delta t}\tilde{\mathbf{u}}_2^{n+1}+\alpha\nu\tilde{\mathbf{u}}_2^{n+1}=-\phi^*\nabla\mu^*.\end{cases} \tag{A.24}$$

We use the split form for the variables μ^{n+1} from (A.1) and $\tilde{\mathbf{u}}^{n+1}$ from (A.23) to rewrite (3.62) as the following form:

$$(\frac{3}{2\delta t}-\theta_2)Q^{n+1}=\frac{1}{2\delta t}(4Q^n-Q^{n-1})+\theta_1, \tag{A.25}$$

where

$$\theta_i=\int_\Omega\Big(\nabla\cdot(\mathbf{u}^*\phi^*)\mu_i^{n+1}+(\phi^*\nabla\mu^*)\cdot\tilde{\mathbf{u}}_i^{n+1}\Big)d\boldsymbol{x}. \tag{A.26}$$

To show (A.25) is solvable, we take the L^2 inner product of (A.24) with $\tilde{\mathbf{u}}_2^{n+1}$, we obtain

$$-\int_\Omega\phi^*\nabla\mu^*\cdot\tilde{\mathbf{u}}_2^{n+1}d\boldsymbol{x}=\tau\frac{a}{2\delta t}\|\tilde{\mathbf{u}}_2^{n+1}\|^2+\alpha\|\sqrt{\nu}\tilde{\mathbf{u}}_2^{n+1}\|^2\geq 0. \tag{A.27}$$

Meanwhile $-\int_\Omega\nabla\cdot(\mathbf{u}^*\phi^*)\mu_2^{n+1}d\boldsymbol{x}\geq 0$ still holds from (A.22). Thus (A.25) is uniquely solvable.

Similar to scheme (3.58)–(3.65), the implementation of the scheme (3.58)–(3.65) is also very simple, where the total expense at each time step includes solving three linear elliptic equations in step 1, and one Poisson-type equation in step 5, and all equations have constant coefficients, thereby implying very efficient practical calculations.

References

[1] J. Rubinstein, P. Sternberg, Nonlocal reaction–diffusion equations and nucleation, IMA J. Appl. Math. 48 (1992) 249–264.
[2] X. Yang, J.J. Feng, C. Liu, J. Shen, Numerical simulations of jet pinching-off and drop formation using an energetic variational phase-field method, J. Comput. Phys. 218 (2006) 417–428.
[3] X. Chen, D. Hilhorst, E. Logak, Mass conserved Allen-Cahn equation and volume preserving mean curvature flow, Interfaces Free Bound. 12 (2010) 527–549.
[4] D.C. Antonopoulou, P.W. Bates, D. Blomker, G.D. Karali, Motion of a droplet for the stochastic mass-conserving Allen-Cahn equation, SIAM J. Math. Anal. 48 (2016) 670–708.
[5] P.E. Kettani, D. Hilhorst, K. Lee, A stochastic mass conserved reaction–diffusion equation with nonlinear diffusion, Discrete Contin. Dyn. Syst. - A 38 (2018) 5615–5648.
[6] Z. Chai, D. Sun, H. Wang, B. Shi, A comparative study of local and nonlocal Allen-Cahn equations with mass conservation, Int. J. Heat Mass Transfer 122 (2018) 631–642.
[7] J. Zhang, X. Yang, Unconditionally energy stable large time stepping method for the L2-gradient flow based ternary phase-field model with precise nonlocal volume conservation, Comput. Methods Appl. Mech. Engrg. 361 (2020) 112743.
[8] J. Zhang, X. Yang, Numerical approximations for a new L2-gradient flow based phase field crystal model with precise nonlocal mass conservation, Comput. Phys. Comm. 243 (2019) 51–67.
[9] X. Yang, A novel fully-decoupled scheme with second-order time accuracy and unconditional energy stability for the navier-stokes equations coupled with mass-conserved allen-cahn phase-field model of two-phase incompressible flow, Internat. J. Numer. Methods Engrg. (2021) http://dx.doi.org/10.1002/nme.6578.
[10] X. Yang, A novel fully-decoupled, second-order and energy stable numerical scheme of the conserved allen-cahn type flow-coupled binary surfactant model, Comput. Methods Appl. Mech. Engrg. 373 (2021) 113502.
[11] X. Yang, Numerical approximations of the navier-stokes equation coupled with volume-conserved multi-phase-field vesicles system: fully-decoupled, linear, unconditionally energy stable and second-order time-accurate numerical scheme, Comput. Methods Appl. Mech. Engrg. 375 (2021) 113600.
[12] J. Kim, S. Lee, Y. Choi, A conservative allen–cahn equation with a space–time dependent lagrange multiplier, Internat. J. Engrg. Sci. 84 (2014) 11–17.
[13] D. Jeong, J. Kim, Conservative allen–cahn–navier–stokes system for incompressible two-phase fluid flows, Comput. & Fluids 156 (2017) 239–246.
[14] P.-H. Chiu, Y.-T. Lin, A conservative phase field method for solving incompressible two-phase flows, J. Comput. Phys. 230 (1) (2011) 185–204.
[15] R. Nochetto, J.-H. Pyo, The gauge-Uzawa finite element method part I: the Navier-Stokes equations, SIAM J. Numer. Anal. 43 (2005) 1043–1068.
[16] J.L. Guermond, P. Minev, J. Shen, An overview of projection methods for incompressible flows, Comput. Methods Appl. Mech. Engrg. 195 (2006) 6011–6045.
[17] R. Rannacher, On chorin's projection method for the incompressible navier-stokes equations, in: Lecture Notes in Mathematics, vol. 1530, 1991.
[18] J.L. Guermond, J. Shen, On the error estimates of rotational pressure-correction projection methods, Math. Comp. 73 (2004) 1719–1737.
[19] J.L. Guermond, A. Salgado, A splitting method for incompressible flows with variable density based on a pressure Poisson equation, J. Comput. Phys. 228 (8) (2009) 2834–2846.
[20] J.L. Guermond, L. Quartapelle, A projection FEM for variable density incompressible flows, J. Comput. Phys. 165 (1) (2000) 167–188.
[21] C. Liu, J. Shen, X. Yang, Decoupled energy stable schemes for a phase-field model of two-phase incompressible flows with variable density, J. Sci. Comput. 62 (2015) 601–622.
[22] J. Shen, X. Yang, A phase-field model and its numerical approximation for two-phase incompressible flows with different densities and viscositites, SIAM J. Sci. Comput. 32 (2010) 1159–1179.
[23] D. Han, X. Wang, A second order in time, decoupled, unconditionally stable numerical scheme for the Cahn–Hilliard–Darcy system, J. Sci. Comput. 14 (2018) 1210–1233.
[24] D. Han, X. Wang, Decoupled energy-law preserving numerical schemes for the cahn–hilliard–darcy system, Numer. Methods Partial Differential Equations 32 (3) (2016) 936–954.
[25] D. Li, Z. Qiao, On second order semi-implicit Fourier spectral methods for 2d Cahn–Hilliard equations, J. Sci. Comput. 70 (2017).
[26] J. Shen, X. Yang, Numerical approximations of Allen–Cahn and Cahn–Hilliard equations, Discrete Contin. Dyn. Sys. A 28 (2010) 1669–1691.
[27] Y. Cai, H. Choi, J. Shen, Error estimates for time discretizations of Cahn–Hilliard and Allen–Cahn phase-field models for two-phase incompressible flows, Numer. Math. 137 (2017) 417–449.
[28] H. Yu, X. Yang, Decoupled energy stable schemes for phase field model with contact lines and variable densities, J. Comput. Phys. 334 (2017) 665–686.
[29] J. Shen, X. Yang, Decoupled, energy stable schemes for phase-field models of two-phase incompressible flows, SIAM J. Numer. Anal. 53 (1) (2015) 279–296.
[30] D. He, K. Pan, An unconditionally stable linearized difference scheme for the fractional Ginzburg-Landau equation, Numer. Algorithms 79 (2018) 899–925, 01.
[31] J. Shen, C. Wang, S. Wang, X. Wang, Second-order convex splitting schemes for gradient flows with ehrlich-schwoebel type energy: application to thin film epitaxy, SIAM J. Numer. Anal. 50 (2012) 105–125.

[32] D.J. Eyre, Unconditionally gradient stable time marching the Cahn-Hilliard equation, in: Computational and Mathematical Models of Microstructural Evolution (San Francisco, CA, 1998), in: Mater. Res. Soc. Sympos. Proc., vol. 529, MRS, 1998, pp. 39–46.
[33] S.M. Wise, C. Wang, J.S. Lowengrub, An energy-stable and convergent finite-difference scheme for the phase field crystal equation, SIAM J. Numer. Anal. 47 (3) (2009) 2269–2288.
[34] Z. Hu, S.M. Wise, C. Wang, J.S. Lowengrub, Stable and efficient finite difference nonlinear-multigrid schemes for the phase field crystal equation, J. Comput. Phys. 228 (2009) 5323–5339.
[35] D. Han, X. Wang, A second order in time, uniquely solvable, unconditionally stable numerical scheme for Cahn–Hilliard–Navier–Stokes equation, J. Comput. Phys. 290 (2015) 139–156.
[36] X. Yang, H. Yu, Efficient second order unconditionally stable schemes for a phase field moving contact line model using an invariant energy quadratization approach, SIAM J. Sci. Comput. 40 (2018) B889–B914.
[37] X. Yang, J. Zhao, Q. Wang, J. Shen, Numerical approximations for a three components Cahn-Hilliard phase-field model based on the invariant energy quadratization method, M3AS: Math. Models Methods Appl. Sci. 27 (2017) 1993–2030.
[38] X. Yang, Linear, first and second order and unconditionally energy stable numerical schemes for the phase field model of homopolymer blends, J. Comput. Phys. 327 (2016) 294–316.
[39] C. Chen, X. Yang, Efficient numerical scheme for a dendritic solidification phase field model with melt convection, J. Comput. Phys. 388 (2019) 41–62.
[40] J. Shen, J. Xu, J. Yang, The scalar auxiliary variable (sav) approach for gradient flows, J. Comput. Phys. 353 (2018) 407–416.
[41] C. Chen, X. Yang, Fast, provably unconditionally energy stable, and second-order accurate algorithms for the anisotropic Cahn-Hilliard model, Comput. Meth. Appl. Mech. Engrg. 351 (2019) 35–59.
[42] Z. Yang, S. Dong, An unconditionally energy-stable scheme based on an implicit auxiliary energy variable for incompressible two-phase flows with different densities involving only precomputable coefficient matrices, J. Comput. Phys. 393 (2018) 229–257.
[43] Q. Du, R.A. Nicolaides, Numerical analysis of a continuum model of phase transition, SIAM J. Numer. Anal. 28 (1991) 13101322.
[44] J. Vaibhav, K.J. Rajeev, A positivity preserving and conservative variational scheme for phase-field modeling of two-phase flows, J. Comput. Phys. 360 (2018) 137–166.
[45] H. Gomez, der Zee Van, G. Kristoffer, Computational phase-field modeling, in: Encyclopedia of Computational Mechanics, second ed., John Wiley & Sons, Ltd, ISBN: 978-1-119-00379-3, 2017.
[46] H. Gomez, V.M. Calo, Y. Bazilevs, T.J.R. Hughes, Isogeometric analystis of the cahn-hilliard phase-field model, Comput. Methods Appl. Mech. Engrg. 197 (2008) 4333–4352.
[47] I. Romero, Thermodynamically consistent time stepping algorithms for nonlinear thermomechanical systems, Internat. J. Numer. Methods Engrg. 79 (2009) 706–732.
[48] X. Wang, L. Ju, Q. Du, Efficient and stable exponential time differencing runge-kutta methods for phase field elastic bending energy models, J. Comput. Phys. 316 (2016) 21–38.
[49] Q. Du, L. Ju, X. Li, Z. Qiao, Maximum principle preserving exponential time differencing schemes for the nonlocal Allen–Cahn equation, SIAM J. Numer. Anal. 57 (2019) 875–898, 01.
[50] S. Wu, Y. Li, Analysis of the Morley element for the Cahn-Hilliard equation and the Hele-Shaw flow, ESAIM: M2AN 54 (2020) 1025–1052.
[51] C. Liu, J. Shen, A phase field model for the mixture of two incompressible fluids and its approximation by a Fourier-spectral method, Physica D 179 (3–4) (2003) 211–228.
[52] J. Shen, X. Yang, Decoupled energy stable schemes for phase filed models of two phase complex fluids, SIAM J. Sci. Comput. 36 (2014) B122–B145.
[53] H. Yu, X. Yang, Numerical approximations for a phase-field moving contact line model with variable densities and viscosities, J. Comput. Phys. 334 (2017) 665–686.
[54] H. Abels, H. Garcke, G. Grün, Thermodynamically consistent, frame indifferent diffuse interface models for incompressible two-phase flows with different densities, Math. Models Methods Appl. Sci. 22 (3) (2012) 1150013, 40.
[55] S. Minjeaud, An unconditionally stable uncoupled scheme for a triphasic Cahn–Hilliard/Navier–Stokes model, Numer. Methods Partial Differential Equations 29 (2) (2013) 584–618.
[56] D. Han, A. Brylev, X. Yang, Z. Tan, Numerical analysis of second order, fully discrete energy stable schemes for phase field models of two phase incompressible flows, J. Sci. Comput. 70 (2017) 965–989.
[57] L. Chen, J. Zhao, A novel second-order linear scheme for the Cahn-Hilliard-Navier–Stokes equations, J. Comput. Phys. (2020) 109782.
[58] Y. Gong, J. Zhao, Q. Wang, Second order fully discrete energy stable methods on staggered grids for hydrodynamic phase field models of binary viscous fluids, SIAM J. Sci. Comput. 40 (2018) B528–B553.
[59] D. Kay, R. Welford, Efficient numerical solution of cahn-hilliard-navier-stokes fluid in 2d, SIAM. J. Sci. Comput. 29 (3) (2007) 2241–2257.
[60] Y. Chen, J. Shen, Efficient, adaptive energy stable schemes for the incompressible cahn–hilliard navier–stokes phase-field models, J. Comput. Phys. 308 (2016) 40–56.
[61] S. Dong, J. Shen, A time-stepping scheme involving constant coefficient matrices for phase-field simulations of two-phase incompressible flows with large density ratios, J. Comput. Phys. 231 (17) (2012) 5788–5804.
[62] Y. Gong, J. Zhao, X.-G. Yang, Q. Wang, Fully discrete second-order linear schemes for hydrodynamic phase field models of binary viscous fluid flows with variable densities, SIAM J. Sci. Comput. 40 (1) (2018) B138–B167.
[63] X. Yang, Efficient linear, stabilized, second order time marching schemes for an anisotropic phase field dendritic crystal growth model, Comput. Methods Appl. Mech. Engrg. 347 (2019) 316–339.
[64] A. Karma, W. Rappel, Phase-field model of dendritic sidebranching with thermal noise, Phys. Rev. E 60 (1999) 3614–3625.

[65] R.H. Nochetto, A.J. Salgado, I. Tomas, A diffuse interface model for two-phase ferrofluid flows, Comput. Meth. Appl. Mech. Engrg. 309 (2016) 497–531.
[66] B.I. Lev, V.G. Nazarenko, A.B. Nych, P.M. Tomchuk, Deformation and instability of nematic drops in an external electric field, JETP Lett. 71 (2000) 262–265.
[67] R.H. Nochetto, A.J. Salgado, S.W. Walker, A diffuse interface model for electrowetting with moving contact lines, Math. Models Methods Appl. Sci. 24 (2014) 67–111.
[68] C. Liu, J. Shen, X. Yang, Dynamics of defect motion in nematic liquid crystal flow: modeling and numerical simulation, Comm. Comput. Phys 2 (2007) 1184–1198.
[69] D.H. Klein, C.J. Garcia-Cervera, H.D. Ceniceros, L.G. Leal, Ericksen number and deborah number cascade predictions of a model for liquid crystalline polymers for simple shear flow, Phys. Fluids 19 (2007) 023101.
[70] Roland Becker, Xiaobing Feng, Andreas Prohl, Finite element approximations of the Ericksen-Leslie model for nematic liquid crystal flow, SIAM J. Numer. Anal. 46 (4) (2008) 1704–1731.
[71] J.J. Feng, C. Liu, J. Shen, P. Yue, An energetic variational formulation with phase field methods for interfacial dynamics of complex fluids: advantages and challenges, IMA Vol. Math. Appl. 140 (2005) 1–26.
[72] J. Bear, Dynamics of Fluids in Porous Media, Courier Dover Publications, New York, 1988.
[73] D.A. Nield, A. Bejan, Convection in Porous Media, second ed., Springer-Verlag, New York, 1999.
[74] J. Shen, X. Yang, The IEQ and SAV approaches and their extensions for a class of highly nonlinear gradient flow systems, Contemp. Math. 754 (2020) 217–245.
[75] J. Shen, J. Xu, J. Yang, A new class of efficient and robust energy stable schemes for gradient flows, SIAM Rev. 61 (2019) 474–506.
[76] A. Diegel, C. Wang, X. Wang, S. Wise, Convergence analysis and error estimates for a second order accurate finite element method for the Cahn-Hilliard-Navier–Stokes system, Numer. Math. 135 (2013) 495–534.
[77] D. Kay, V. Styles, R. Welford, Finite element approximation of a Cahn-Hilliard-Navier–Stokes system, Interfaces Free Bound. 10 (2008) 15–43.
[78] J. Shen, X. Yang, H. Yu, Efficient energy stable numerical schemes for a phase field moving contact line model, J. Comput. Phys. 284 (2015) 617–630.
[79] F. Guillen-Gonzalez, G. Tierra, Unconditionally energy stable numerical schemes for phase-field vesicle membrane model, J. Comput. Phys. 354 (2018) 67–85.
[80] J. Shen, Efficient spectral-Galerkin method I. direct solvers for second- and fourth-order equations by using Legendre polynomials, SIAM J. Sci. Comput. 15 (1994) 1489–1505.
[81] C. Yuan, H. Zhang, Self-consistent mean field model of hydrogel and its numerical simulation, J. Theoret. Comput. Chem. 12 (2013) 1350048.
[82] A.K. Forster, J. Khandpur, S. Zhao, F.S. Bates, Complex phase behavior of polyisoprene-polystyrene diblock copolymers near the order–disorder transition, Macromolecules 27 (1994) 6922–6935.
[83] O. Wodo, B. Ganapathysubramanian, Computationally efficient solution to the cahn-hilliard equation: Adaptive implicit time schemes, mesh sensitivity analysis and the 3d isoperimetric problem, J. Comput. Phys. 230 (15) (2011) 6037–6060.
[84] J.-D. Chen, Growth of radial viscous fingers in a Hele-Shaw cell, J. Fluid Mech. 201 (1989) 223–242.
[85] R. Tsuzuki, Q. Li, Y. Nagatsu, C.-Y. Chen, Numerical study of immiscible viscous fingering in chemically reactive Hele-Shaw flows: Production of surfactants, Phys. Rev. Fluids 4 (2019) 104003.
[86] P.G. Saffman, G. Taylor, The penetration of a fluid into a porous medium or Hele-Shaw cell containing a more viscous liquid, Proc. R. Soc. Lond. Ser. A Math. Phys. Eng. Sci. 245 (1958) 312329.